BEHAVIOR OF NEURO-2A CELLS ON FEMTOSECOND LASER STRUCTURED SILICON SUBSTRATES

A THESIS SUBMITTED TO
THE GRADUATE SCHOOL OF NATURAL AND APPLIED SCIENCES
OF
MIDDLE EAST TECHNICAL UNIVERSITY

BY

SARA MINGU

IN PARTIAL FULFILLMENT OF THE REQUIREMENTS
FOR
THE DEGREE OF MASTER OF SCIENCE
IN
MICRO AND NANOTECHNOLOGY

JULY 2020

Approval of the thesis:

BEHAVIOR OF NEURO-2A CELLS ON FEMTOSECOND LASER STRUCTURED SILICON SUBSTRATES

submitted by **SARA MINGU** in partial fulfillment of the requirements for the degree of **Master of Science in Micro and Nanotechnology Department, Middle East Technical University** by,

Prof. Dr. Halil Kalıpçılar
Dean, Graduate School of **Natural and Applied Sciences** _____

Prof. Dr. Almıla Güvenç Yazıcıoğlu
Head of Department, **Micro and Nanotechnology** _____

Assoc. Prof. Dr. Alpan Bek
Supervisor, **Physics, METU** _____

Assoc. Prof. Dr. Çağdaş Devrim Son
Co-supervisor, **Biological Sciences, METU** _____

Examining Committee Members:

Prof. Dr. Ayşe Eser Elçin
Stem Cell Institute, Ankara University _____

Assoc. Prof. Dr. Alpan Bek
Physics, METU _____

Assoc. Prof. Dr. Çağdaş Devrim Son
Biological Sciences, METU _____

Assoc. Prof. Dr. Filiz Korkmaz Özkan
Physics, Atılım University _____

Assist. Prof. Dr. Ihor Pavlov
Physics, METU _____

Date:

I hereby declare that all information in this document has been obtained and presented in accordance with academic rules and ethical conduct. I also declare that, as required by these rules and conduct, I have fully cited and referenced all material and results that are not original to this work.

Name, Surname: Sara Mingu

Signature :

ABSTRACT

BEHAVIOR OF NEURO-2A CELLS ON FEMTOSECOND LASER STRUCTURED SILICON SUBSTRATES

Mingu, Sara
M.S., Department of Micro and Nanotechnology
Supervisor: Assoc. Prof. Dr. Alpan Bek
Co-Supervisor: Assoc. Prof. Dr. Çağdaş Devrim Son

July 2020, 86 pages

Cells are known to interact with their physical environment and respond to cues such as substrate topography. Knowledge of the cell responses to topography may give information about cell behavior in health and disease, as well as be exploited in order to exert control on cells for various purposes. Cell responses to topography are dependent on cell type, substrate material and topographical features. In the present study, Neuro-2a cell line was used as a versatile and widely available neuronal cell model. The substrates consisted of polished or laser-structured silicon. Structuring was performed using an ultrafast infrared pulsed laser, which generated topographies such as laser induced periodic surface structures (LIPSS) and microcolumns. The substrates were characterized with scanning electron microscopy (SEM). Cells were grown on control substrates (glass or plastic), polished silicon and laser-structured silicon of different topographies for 3 hours or 24 hours to evaluate various cell behaviors. Initial cell adhesion and initial motility, as well as cell adhesion and shape after 24 hours were studied in different substrates using fluorescence microscopy and SEM. Initial cell adhesion was found to be strongest on the microcolumn topography, allowing for

selective cell patterning on microcolumn regions. After 24 hours, cell adhesion was found to be equal in all topographies. Moreover, cell motility was found to be fastest in polished silicon, and slowest in the microcolumn topography. On the other hand, cell area and perimeter was found to be larger on polished silicon and LIPSS, compared to microcolumn topography or glass. No difference was found in the average cell circularity for all substrates. Finally, cell preference for microcolumn stripes was found to be more prominent when LIPSS was found between the stripes, compared to when thee stripes were separated by flat regions. In conclusion, different cell behaviors related to spreading, migration and adhesion were found to be dependent on the substrate topography. Topography on silicon may be promising to control these behaviors in the Neuro-2A cell line.

Keywords: Neuro-2A cells, surface topography, silicon, imaging

ÖZ

NEURO-2A HÜCRELERİNİN FEMTOSANİYE LAZER İLE İŞLENMİS SİLİKON YÜZEYLERİNİN ÜSTÜNDEKİ DAVRANIŞLARI

Mingu, Sara
Yüksek Lisans, Mikro ve Nanoteknoloji Bölümü
Tez Yöneticisi: Doç. Dr. Alpan Bek
Ortak Tez Yöneticisi: Doç. Dr. Çağdaş Devrim Son

Temmuz 2020 , 86 sayfa

Hücrelerin bulundukları fiziksel ortama ve özellikle yüzeylerin topografik işaretlerine tepki verdikleri gözlemlenmiştir. Hücrelerin bu işaretlere verdiği tepkilerin keşfedilmesi, hücrelerin normal aktiviteleriyle ilgili bilgi verebilir yada hücrelerin davranışları üstünde kontrol sağlayabilir. Hücrelerin topografiye olan tepkileri; hücre türüne, substrat malzemesine ve topografik özelliklerine bağlıdır. Bu çalışmada, kullanımı ve bulunması kolay olan Neuro-2a hücre hattı kullanılmıştır. Hücre kültürü substratı olarak ise silikon malzemesi kullanılmıştır. Silikon yüzeyi lazer ile işlenerek mikrokolonlar ya da lazerle yapılmış periyodik yüzey yapıları (LIPSS) oluşturulmuştur. Yüzeyler, taramalı elektron mikroskobu ya da atomik kuvvet mikroskobu kullanarak karakterize edilmiştir. Hücreler, 3 ya da 24 saat boyunca işlenmiş yüzeyler üstünde büyütülmüştür ve davranışları cilalı silikon ya da plastik veya cam yüzeylerle kıyaslanmıştır. Hücre şekilleri, sayıları ve hareketleri taramalı elektron mikroskop ya da konfokal floresan mikroskop kullanılarak gözlemlenmiştir. İlk saatlerde hücreler en güçlü şekilde mikrokolon topografisine bağlanmıştır. Bunu gözlem, hücreleri subst-

ratların belli yerlerine sınırlandırmak için kullanılmıştır. 24 saat sonra ise hücreler bütün silikon topografilerine eşit şekilde bağlanmıştır. Hücre hareketlerinin, cilalı silikonda en hızlı, mikrokolonlarda ise en yavaş olduğu gözlemlenmiştir. Hücre şekillerinin de değişiklik gösterdiği; cilali silikon ve LIPSS yüzeylerde hücre yüzey alanı ve çevre uzunluğu, mikrokolon ve camdaki hücrelerle kıyasla daha büyük olduğu gözlemlenmiştir. Son olarak, LIPSS ya da cilali yüzey üstüne mikrokolonlardan oluşan çizgileri olan yüzeylerde, hücrelerin farklı tepkileri gözlemlenmiştir. Hücreler, LIPPS olan yüzeylerde çizgilerin üstüne yerleştiği görülürken, cilalı alanları olan yüzeylerdeki hücrelerin mikrokolon çizgilerin üstüne yerleşmediği görülmüştür. Özet olarak, hücrelerin farklı davrasnışlarının yüzey topografisine bağlı olarak değiştiği gösterilmiştir. Silikon üstünde topografi, hücrelerin yayılımını, hareketlerini ve yapışmasını kontrol etmek için umut vadeden bir yaklaşım olabilir.

Anahtar Kelimeler: Neuro-2A hücreleri, yüzey topografisi, silikon, görüntüleme

To everyone who trusted and supported me throughout these years,
and for everyone who will benefit from this work.

ACKNOWLEDGMENTS

This work taught me, besides many other things, the importance of communication and collaboration in scientific research. I want to thank so many people for all the help I have received throughout these years.

First of all, my deepest appreciation and gratitude go to the principal investigators I worked with.

My advisor, Assoc. Prof. Dr. Alpan Bek, put the whole idea forward; he introduced and guided me on all the structuring and characterization techniques, and provided numerous ideas and suggestions for this thesis. He motivated and encouraged me to present this work at both a national and an international conference, and taught me so much about scientific collaboration, scientific writing and publishing. I am grateful to him for trusting me with this project, guiding me along the way, and motivating my first conference poster, first presentation, and first publication and all my other very first steps into this journey. I will also always happily remember all the cheerful and inspiring conversations we had in these years, not only about this project, but also about academic career, and what it means to be a scientist.

My co-advisor, Assoc. Prof. Dr. Çağdaş Devrim Son, welcomed me as a MSc student in his laboratory, where I carried out all the cell experiments, molecular biology procedures, and imaging. He taught me all I know about cell biology, fluorescence and microscopy. He guided me on all the biology components of the project, helped me interpret all the data, and suggested the best ways to proceed in order to optimize this project for the laboratory. I want to thank him for all his trust, patience and support.

Assist. Prof. Dr. Ihor Pavlov built and maintained the femtosecond laser, helped me with all the structuring, and offered various new leads and ideas to try. His enthusiasm about this project and his ideas have motivated many of the results presented here, as well as further work in progress.

I have been extremely lucky to work with these wonderful advisors. They gave me the right amount of freedom to discover and pursue this project, and always full support and motivation to carry on, even when I lost hope. I owe this all to them, and if i am to continue in this journey, it is because they supported me and made me realize what an inspiring career it can be.

I want to thank Prof. Dr. Eser Elçin for helping me interpret data, as well as offering valuable suggestions for my thesis, being in my jury, and offering her advice and suggestions even afterwards. At the same time, I would like to thank Assoc. Prof. Dr. Filiz Korkmaz Özkan for being in my jury and offering her support, which meant a lot to me in this stressful period. I am grateful to have had them in my thesis committee, and thankful for their comments and suggestions to improve this work.

In the Nano-Optics group in the Physics Department, Firat İdikut helped me with the laser operation and safety in all the laser structuring procedures. He taught me a lot about the laser operation and optics and always assisted me in this work. For the operation of Atomic Force Microscopy, I would like to thank Mona Borra and İbrahim Murat Öztürk, who taught me how to use the instrument and helped me take good scans of my samples. For Scanning Electron Microscopy, I want to thank Nardin Avishan for giving me training, and İbrahim Murat Öztürk, Nasim Seyedpour and Özün Candemir for taking SEMs of my samples. I want to additionally thank Özün Candemir for her help with laser operation, and Behrad Radfar for all wafer slicing. Finally, I would like to thank the Phys400 students who worked with me as part of their Special Project, Elifcan Göktepe and Ezgi Şamli, for all the experiments they helped with.

In the Biology Department, I want to thank all the past and present members of the lab for their assistance. When I first came to the lab, Özge Atay and Hüseyin Evci taught me all the protocols and procedures. I want to thank them for their help, and additionally thank Hüseyin for the preparation of the Gap43 and NLS tagged constructs, which I have used in this study. I would also like to thank all current members of the lab, for all their help. Ali, Enise, Seyda, thank you for all the times you seeded cells for me, picked up my primers or mail, lended me agar plates, LB, chemicals, and everything else. Ali in particular helped me with experiments often,

and always taught me details about the protocols I used. He always motivated me to research the details of the protocols, and for this I will always remember him. I would also like to thank Şeyda Çulfa for her enthusiasm and help in the experiments recently, and wish her luck in the continuation of her work.

I would also like to thank the members of our partner lab in Ankara University Stem Cell institute. I would like to thank Dr. Orkun Cevheroğlu for his kindness, his patience and for teaching me so much about molecular cloning, microscopy, and many more procedures and instruments. I would also like to thank Merve Murat, who likewise taught and supported me in all molecular cloning procedures, helped with the experiments whenever I needed, and has been a great friend to me. And even though we only started to work together recently, I also want to thank Nil Demir for her friendship and her support. I have been at luck to have amazing lab mates. At the Stem Cell Institute, I would also like to thank Assist. Prof. Dr. Şükran Şeker for helping me interpret cell images.

Finally, I want to thank everyone who motivated and assisted me throughout these years in my personal life. My friends, my family and my husband have supported and motivated me constantly throughout these years, each in their own unique ways.

My friends have always offered their motivating words, and made me feel happy and loved. I want to give a special thanks to Samet Aytekin, for knowing and saying the words I need to hear, always.

My family gave me a wonderful childhood, and provided me with all the support and freedom to pursue my dreams throughout my life - the greatest gifts one could ever have.

My husband, Atakan Tuğberk Akmete, has always supported me during this study, stayed up with me at the lab numerous times, and always motivated me to continue, to improve, to overcome myself. I look forward to a life full of exploring, discovering and learning, with him.

TABLE OF CONTENTS

LIST OF TABLES

TABLES

LIST OF FIGURES

FIGURES

LIST OF ABBREVIATIONS

ABBREVIATIONS

1D	1 Dimensional
2D	2 Dimensional
3D	3 Dimensional
4 %FA	4%formaldehyde solution
AFM	Atomic force microscopy
CZ	Czochralski Method
DMEM	Dulbecco's modified eagle medium
ECM	Extracellular matrix
EGFP	Enhanced Green Fluorescent Protein
eV	Electron-Volt
FBS	Fetal bovine serum
LB	Lysogeny broth
LIPSS	Laser-induced periodic surface structures
PCR	Polymerase chain reaction
SEM	Scanning electron microscopy
SPP	Surface plasmon polariton

CHAPTER 1

INTRODUCTION

1.1 Rationale for studying cell-substrate interactions

The cells are known to interact with their environment and respond to different cues. This is not a trivial fact; the success of all medical implants, as well as the possibility of advancing organ-on-a-chip, artificial organs, tissue engineering and regenerative medicine applications depends on the proper knowledge of the cell responses to the environmental cues, and the utilization of this knowledge to obtain the desired results. Here, environmental cues is a term comprising all kinds of signals the cells may get from their environment. These may include the presence of certain molecules in the environment (small molecules, proteins, even other cells), environmental rigidity/elasticity and topography. Each type of cue may have a specific effect on a specific cell type, and different types of cues may have synergistic effects. Using a reductionist approach, specific types of cues may be studied separately.

In the present work, only topographical cues have been considered, using a model cell on a model substrate. Although the study falls under basic research, it is hoped that the observed cell behavior patterns may become useful for future applications.

1.2 The cell at a glance

Cells are composed of various compartments and numerous proteins and protein complexes which mediate their many behaviors. All cells are surrounded by a membrane, which is composed of a lipid bilayer with numerous different protein receptors integrated in it (transmembrane proteins). A typical cell can range from 10 μm to 50 μm

in diameter, depending on the cell type.

1.2.1 The actin cytoskeleton and stress fibers

In the inner part of the cell, a dynamic network of fibrous proteins called the cytoskeleton is responsible for giving cells shape and rigidity, as well as for performing several other functions. The cytoskeleton is comprised of three different networks: the actin cytoskeleton, microtubules and intermediate filaments; each of these has their specific functions and dynamics. The actin cytoskeleton in particular has been shown to mediate various cell interactions with the substrates, and it is commonly observed in cell-substrate interaction studies. Actin is a globular protein which can polymerize into filaments and depolymerize. Several proteins are known to interact with the actin monomers or filaments, and affect polymerization/depolymerization, the arrangement of the actin filaments into bundles or networks, as well as their movements. For example, myosin is a common protein which interacts with actin filaments by pulling them against each other in order to generate force. Actin polymerization is promoted by several proteins, and it is an important initial step for cell spreading on the substrates, as well as for the force generation needed for membrane protrusions. Other proteins (myosin, α-actinin) mediate the interaction of individual actin filaments, joining 10-30 of them together in parallel fashion in larger bundles called stress fibers. Stress fibers are contractile structures consisting of several types and important for cell interaction with the extracellular matrix (ECM).

1.2.2 Filopodia and lamellipodia

The actin cytoskeleton is involved in different protrusions important for substrate or ECM sensing. Filopodia are finger-like projections of the cytoskeleton with diameters of 100-300 nm. They are composed of 12-20 actin filaments and are highly stable. Filopodia are sensors of the microenvironment [5]. For example, filopodia are used for sensing the surface features of neighbor cells during embryo development.

Lamellipodia, on the other hand, are sheet-like projections driven by actin polymerization and cross-linking by the Arp2/3 complex. As such, the lamellipodia contain a

mesh-like actin network. They are formed by extensions and retractions of the leading edge of the cell, and have roles in cell motility [5].

1.2.3 Integrins and focal adhesions

Some cell surface receptors, such as integrins, interact with the cytoskeleton and mediate many relevant responses of cells to ECM or substrates. Integrins are heterodimeric proteins composed of different subunits, α and β. These subunits may have different signaling and adhesive properties. Cells may express various subunits at different amounts and can change the repertoire of expressed integrin subunits according to environmental signals, and even topography. The integrins interact with the cytoskeleton through various other proteins. In particular, the points of interaction of integrins with actin stress fibers are composed of a complex protein network called the focal adhesion. Focal adhesions are found at the periphery and also at other positions closer to the center at the lower membrane of cells adhering on the substrates. These structures are of great importance in the cell response to the substrate topography, and focal adhesion size or shape is commonly looked at in cell-substrate interaction studies. The molecular structure of the focal adhesion has been elucidated [1], it is known to contain integrins, focal adhesion kinase and paxillin (integrin signaling layer); talin and vinculin (force transduction layer); and zyxin and α-actinin (actin regulatory layer). A scheme of the focal adhesion is shown in Figure 1.1.

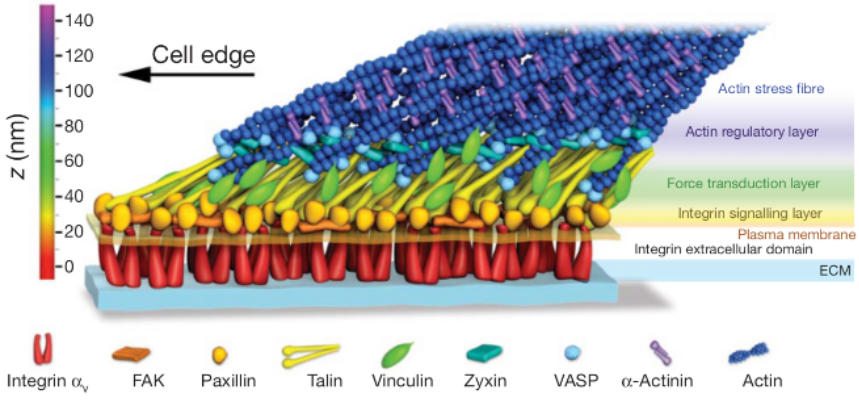

Figure 1.1: Nanoscale architecture of focal adhesions. Adapted from [1].

Several of these proteins play a role in cell responses to substrate topography and

may also signal through other pathways in order to affect cell cycle, differentiation or apoptosis (cell death). Many studies of cell-substrate interactions use antibodies against these proteins in order to study the focal adhesions of cells on different topographies.

1.2.4 Events in cell spreading

The early events in cell spreading have been described in literature [6]. Observation of cells during attachment to substrate shows that cell adhesion occurs in three major phases:

- Initial attachment through integrin clustering
- Rapid increase in cell spread area through the depletion of cell membrane reservoirs
- Slower spreading through periodic protrusion and retraction of cell edge and increase in membrane area

Before reaching the surface, cells are spherical in shape and their membrane is heavily folded. When the cells reach the surface, integrin receptors on their surface start to interact with specific motifs on the adsorbed ECM proteins. If the motifs displayed on the substrate are appropriately spaced, the integrins at the leading edge (the edge of the cell membrane making contact with the substrate) start to cluster together, providing both strength and maturation of the nascent adhesion. The clustering of integrins is an essential first step for the spreading of the cells, and necessitates appropriate distribution of binding motifs, such as the Arginine-Glycine-Aspartic acid motif (RGD). Next, the cell applies force to these nascent adhesions through its cytoskeleton in a process involving actin and myosin. This force is not necessary for integrin clustering but essential for the further adhesion maturation steps. The adsorption strength of the proteins to the surface and the substrate rigidity become relevant in this step. The integrin clusters dissipate if force is not developed on them. If force develops, this force-dependent activation allows the progression of cell spreading. The membrane, which had been folded in the prior stages, starts to spread out. The cell shape changes

from spherical to flattened out. The process is known to involve actin polymerization from the initial integrin clusters. The membrane flattening increases membrane tension and activates myosin-dependent contractility. This behavior continues after the first stages, with cells periodically spreading lamellipodia in order to test the substrate rigidity. Inability to generate enough force inhibits further spreading. After cell spreading is complete, several different behaviors such as migration, division or differentiation may take place. These behaviors are strictly regulated by many different proteins and may be affected by the substrate topography.

1.2.5 Overview of cell behaviors

Cell migration refers to cell movement on the substrate. It is a common cell behavior; cells will move around at random if no cues are present, or towards a chemical gradient if available. Cell migration involves the cytoskeleton as well as the adhesions. The cell extends a lamellipodium, and adhesions start to form at its edge (the leading edge). A schematic representation of cell motility is shown in Figure 1.2.

Cell migration may be dependent on the substrate. For example, cells migrate from soft to hard (rigid) substrate regions, a process called durotaxis. Some topographical cues may elicit directional migration.

Cell division is a highly regulated process in which cells divide into two daughter cells. Cell proliferation (or cell growth) refers to a net increase in the cell number, through divisions outnumbering cell death. For cell-substrate interactions, cell proliferation reflects a positive cell response to the substrates.

Cell differentiation refers to a specialization of the cell towards a specific lineage (for example, neural cells) accompanied by a loss of division potential. Cells which differentiate develop highly specific functions, such as projections, electrical activity or secretion of specific proteins. Cells which have not differentiated, on the other hand, retain their proliferative potential. In particular, stem cells are cells which have not differentiated yet and have the potential to differentiate into multiple cell types. Their differentiation into various lineages and the factors affecting it are important for basic science as well as for many applications.

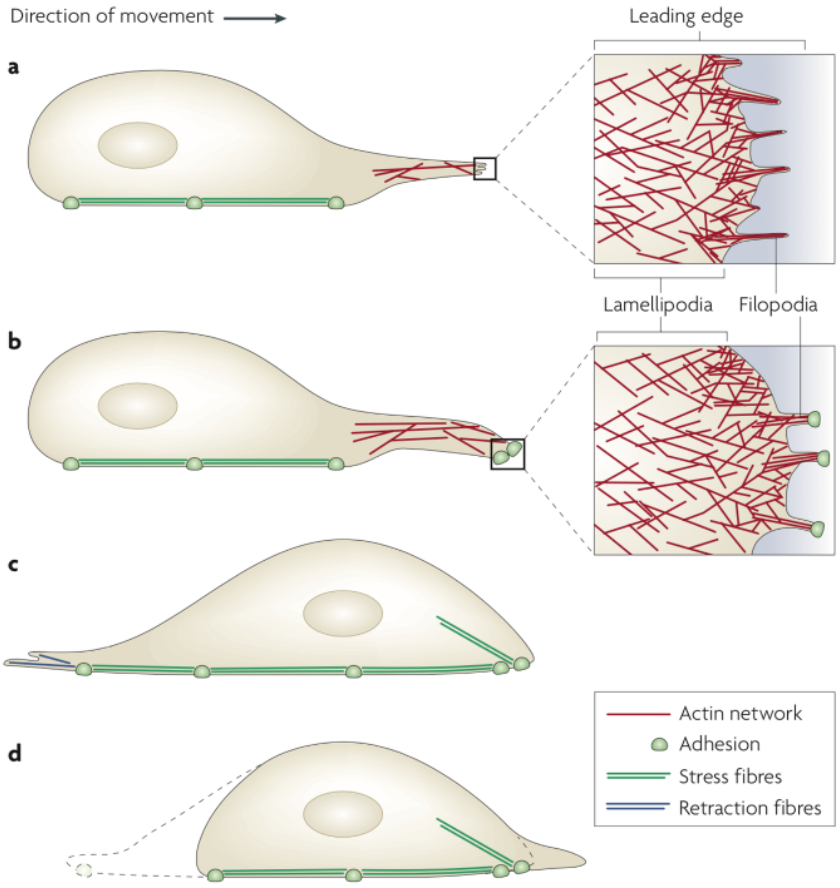

Figure 1.2: Schematic representation of cell motility, showing the leading edge, lamellipodia and filopodia. [2].

1.2.6 Effects of topography on cell behaviors

Nanotopography can affect cell spreading and adhesion, usually in a cell and material-dependent manner. For example, SH-SY5Y cells responded negatively to isotropic roughness on gold; roughness down to Ra values of 40 nm inhibited focal adhesions and led to loss of polarization and necrosis. This effect was used to generate cytophilic and cytophobic areas on the same substrate [7]. Laser treatment of stainless steel was shown to change the wettability characteristics and surface energy of the material, and increase the adhesion and spreading of osteoblasts compared to both untreated and mechanically roughened surfaces [8]. In another study involving MCF7 cells on patterned poly-L-lactic acid (PLLA) films, it was found that a particular subpopulation of the cells (the $CD44^{+}CD24^{-/low}ESA^{+}$ subpopulation) preferentially adhered

to 350 nm gratings. Specific enrichment, isolation and characterization of cancer stem cells could therefore be possible by using topography as a selection [9]. Laser irradiation of Ti6Al4V alloy and the formation of microgrooves was found to increase its biocompatibility, affect wettability and protein adsorption on the surface, and increase the viability and spreading of MG63 cells [10]. Fibroblast cells grown on PMMA nanocolumns of 100 nm diameter and 160 nm height showed a decrease in cell perimeter and an increase in filopodia number/μm perimeter. Their filopodia was seen to interact with the environment [11]. The importance of the physical environment and topography was emphasized by a study on neuronal cells. The substrates were glass slides covered with silica nanoparticles of controlled size. It was found that a roughness (Rq) of 32 nm (corresponding to the roughness of healthy astrocytes) caused the dissociation of hippocampal neurons from astrocytes in a co-culture study, underlining the importance of nanotopography in the interactions between neurons and astrocytes [12].

Isotropic substrates may also affect cell alignment. Gratings of width 1 μm and depths of 1 μm or more on olefin copolymer foils were found to speed up endothelial cell spreading and elicit their alignment [13]. PC12 cells induced with NGF showed neurite alignment and guided movement on grating-like structures on polystyrene with 200 nm depth and 500 or 1000 nm linewidth. Leech neurons were found to interact with grating topographies on plastic, by polarization of their tubulin cytoskeleton in the direction of the grating. The substrates had 350 nm depth and 1 μm or 2 μm width and were made using pattern transfer from silicon molds fabricated using electron beam lithography. The topography sensing was suggested to take place through filopodia. A comparison to other neuronal cell lines (PC12, SH-SY5Y, F11, differentiated mouse embryonic stem cells and murine hippocampal neurons) showed that all cell types showed neurite alignment to grating topographies of the two widths [14]. Primary culture neurons grown on grating topographies on glass showed a correlation between ridge height and neurite alignment. The influence of the ridges on the neurite was defined as a change in the neurite direction through temporal interaction with the ridge. About half the neurites interacted with 25 nm high ridges while 80% interacted with 100 nm high ones, emphasizing the importance of the grating depth in eliciting alignment responses [15]. In another study, different ridge and groove sizes of grat-

ing topographies on cyclic-olefin-copolymer films were found to influence polarity (number of neurites) and alignment of neurons; the effect being related to the focal adhesion formation onto the ridge structures [13]. Finally, in one study, neurons were grown on a substrate with nanopillars of different sizes in specific locations. Neurons interacted with the topographical cues by engulfing them with their cell body or protrusions. Moreover, neurons which interacted with the nanopillars were less likely to migrate; in that sense, nano-pillars allowed for the non-invasive "pinning" of neural cells [16].

Some topographies can induce or enhance cell proliferation for certain cell types. For example, osteoblasts were able to adhere, grow and proliferate on vertically aligned TiO_2 nanotubes formed by anodization. Proliferation rate was shown to increase by 3-4 times on this topography [17]. Nano-pit topography consisting of 120 nm pits of square arrangement with 300 nm side length was shown to affect the cell cycle in skeletal stem cells, and permit the cells' proliferation together with multipotency retention [18]. TiO_2 nanotubes were shown to be better for osteoblast adhesion than both polished and etched Ti. The osteoblast response was attributed to the high roughness, high hydrophilicity and high surface energy of the substrates. Cell proliferation, osteoblastic phenotype expression and adhesion were all improved [19].

Some topographies, on the other hand, enhanced cell differentiation. In one study, authors generated a multiple-architecture chip comprising various topographies to find the optimal topography for neural progenitor cell differentiation. Among numerous topographies, 2 μm and 250 nm anisotropic gratings were found to promote neural differentiation whereas 2 μm holes and 1 μm pillars promoted glial differentiation [20]. Multiple-architecture chip with different topographies was used in one study to find optimal topographies to modulate neuronal or glial differentiation of embryonic stem cells (hESCs). It was found that neuronal differentiation is promoted by anisotropic patterns such as gratings while glial differentiation by isotropic topographies such as pillars [21]. Nano-pit topography on polycaprolactone (PCL) was shown to affect differentiation of skeletal stem cells. Highly regular 120 nm pits in a square arrangement with distance 300 nm was shown to increase retention of MSC markers and multipotency; on the other hand, offsets in pit placement (resulting in more irregular square lattice structures) enhanced osteogenic differentiation [22].

Collagen-fibroin blend films with microchannel topography of 4.8 μm ridge width, 10.8 μm groove width and 4 μm depth was found to increase the aspect ratio, alignment and osteogenic differentiation of adipose derived stem cells [23].

Some studies have looked at the changes in gene or protein expression elicited by topography, in order to shed more light on the cell responses. In PC12 cells, nanotopography was shown to affect various proteins involved in processes like cell-cell interaction, ECM, membrane/f-actin linkage, integrin activation, cytoskeleton, nuclear organization and transcriptional regulation. In particular, ILK, mTOR, Wnt and calcium signaling pathways were affected [24]. One study compared the responses of human embryonic stem cells (hESCs) and mesenchymal stem cells (hMSCs) on nanotopographies using multi-architecture chips in order to shed light on mechanotransduction pathways and topography-mediated differentiation. The two cell types showed differences in the expression levels of lamin A/C and histone methylation protein H3K9me3 among each other and on topographies. In particular, hMSCs had a significant increase in H3K9me3 in the first 24 hours of seeding onto 250 nm nanogratings, pointing to possible differentiation pathways on nanotopography [25]. The fibroblast response to 13-nm nanoislands on polymer-demixed polystyrene and polybromostyrene was evaluated using microscopy and microarray expression. On the nanoislands topography, up-regulation of genes involved in cell signaling, proliferation, cytoskeleton and ECM production was observed. In agreement, microscopy images revealed a higher number of filopodia interacting with the substrate, as well as better cell spreading and higher number of focal adhesions [26]. Integrin subunit expression was shown to be affected by nanotopography. Human mesenchymal stem cells (hMSCs) aligned their actin cytoskeleton in the direction of a 350-nm grating topography on PDMS and TCPS. Meanwhile, expression of α2, α6, αV, β2, β3 and β4 integrin subunits decreased compared to control substrates [27].

Neuro-2a is a widely used commercially available cell line. It is commonly used in cell-substrate interaction studies as a model cell line for neuronal cells, in order to study neuronal cell response to different topographies. This cell line is used in the present work. This cell line has many advantages as a neuronal cell model. They are widely available and easy to grow and handle. Neuro-2a cells have been characterized and used widely. Upon differentiation, they are able to show neuron-like

characteristics, and differentiation can be induced with well-known methods such as serum starvation. This allows to reduce the use of primary cells, which have to come directly from the animals and which can only be used a limited amount of time. Neuro-2a cells have been shown to interact positively with cell culture substrates and do not require intricate growth systems like astrocytes or other feeder cultures. They can be sustained on standard cell culture dishes for a few months. For these reasons, Neuro-2a have been chosen in the present study and also in other similar studies as model cells to evaluate the response of neuronal cells to candidate substrate materials. Previous reports of Neuro-2a cell behavior on various materials and topographies are available in the literature. For example, in one study, PDMS neurochips were developed which allowed specific positioning and differentiation of Neuro-2a cells into definite synthetic neural networks [28]. A neurochip for Neuro-2a cells was prepared by replicating PDMS over a silicon mold fabricated with lithographic techniques. The chip was then chemically treated in order to render some parts hydrophilic and some parts hydrophobic. Neuro-2a cells adhered preferentially to hydrophilic surfaces and were able to differentiate into viable neuronal networks in highly defined regions [28]. Reviews of the responses of various neural cells to different topographies are available. Khan and Newaz underline some important results and present hypotheses on the mechanism of cell response to materials and topographies [29].

It is understandable from the various examples above that cell responses are highly dependent on the substrate material, topography and cell type. It is difficult to predict the cell responses to the topography in a theoretical manner, and there seem to be few general trends when it comes to how a specific cell will interact with a specific topography. The response depends on various factors, such as the cell type, age and state, as well as surface chemistry, surface topography, and further modifications.

There seems to be a cell-dependent optimal size for eliciting maximal response by the cell's body or cell parts [30]. Usually, the feature size should be comparable to the size of the cell part with which it will interact. For example, the cell body is usually between 10-50 micrometers and topographical features of this size may confine the whole cell or enhance its elongation or alignment. On the other hand, smaller features may interact with more specific parts of the cells. Filopodia have sizes of 100-300 nm, and several studies have probed the interaction of the filopodia

with topographical features. The height limit of filopodial sensing was found to be 8 nm. The distance limit for integrin clustering was found to be 70 nm; if binding molecules on the substrate are positioned more than 70 nm apart, the integrins are not able to cluster and the cell is not able to anchor itself onto the substrate.

The importance of focal adhesions in mediating the cell response has also been described in various studies. Focal adhesions may be confined by sharp features such as gratings and pillars. On gratings, the focal adhesions may be confined to grow in elliptical shape, rather than circular. Contact guidance and cell polarization may occur due to the alignment of individual focal adhesions and protrusions. For example, in a study using 2D fibrillar substrates, it was found that adhesions formed preferentially in the direction of the fibers, whereas gaps between fibers prevented sequential adhesion formation. In turn, the alignment of several protrusions polarized the entire cell [31]. A study of 3T3 fibroblast cells on micron-sized pillar topography shed some light on the role of myosin and focal adhesion kinase (FAK) on the cell response to the topography. Cell response included a more branched shape, higher speed and lower directionality on the micropillars. It was suggested that an increase in surface contact on the structured surfaces regulates adhesion strength and contraction through myosin II and FAK, and results in the cell responses [32]. One group used nano-line gratings and nanopillars of different sizes to study the assembly and disassembly of focal adhesion protein paxillin. Cell motility was found to be highest on the smallest nanopillars, where focal adhesions were composed of sparser, mostly dimeric paxillin complexes. On the other hand, on larger nanopillars larger focal adhesions with higher order paxillin aggregates provided greater temporal stability and less migration [33]. Alongside signal transduction through focal adhesion proteins, it has been suggested that forces encountered by the cells while spreading on different topographies may also be directly transferred to the nucleus through the cytoskeleton. This, in turn, may affect the positioning of interphase chromosomes and ultimately gene expression [11].

The role of protein adsorption on cell response has also been well described. Cells do not make direct contact with the substrate's surface but rather with proteins adsorbed onto it [34, 35]. The composition of the adsorbed layer mediates the cell behavior. Similar to cells in their native environment, adherent cells in vitro are anchored to

the ECM proteins on the surface of their substrate. The conformational changes that occur during protein adsorption to the substrate surface must allow the display of motifs cells can recognize, if cells are to attach to the surface.

The events leading to cell adhesion to the substrate have been described in literature. Initially, a cell suspension or media only is dropped on the substrate, In the nanosecond scale, water molecules interact with the substrate. This interaction is dependent on the surface properties. A "water shell" forms at the substrate surface. Soluble proteins, which also have their water shell, arrive at the substrate surface next, and interact with the surface in the process of adsorption. Protein adsorption involves the partial dehydration of the protein and the sorbent surface, surface charge group redistribution and possible conformational changes of the protein. For hydrophobic surfaces, displacement of the water layer from the surface is thermodynamically favorable; the hydrophobic parts of proteins may be adsorbed onto the surface through hydrophobic interactions. For hydrophilic surfaces, displacement of the water layer is more unfavorable due to the tight interaction between the water and the surface; nevertheless, protein adsorption is possible, and it is mostly fueled by energy from protein conformational changes. The adsorbed ECM proteins usually come from the cell culture medium serum, such as FBS. In particular, fibronectin and vitronectin are two important such ECM proteins. The adsorption properties of common ECM proteins onto different materials have been studied, and it has been shown that these proteins show different adsorption and conformations on surfaces depending on wettability and charge. In general, hydrophilic surfaces adsorb more protein in the correct conformation, and therefore can better support cell growth. Fibronectin adsorbs on hydrophobic surfaces but with a reduction in functionality. Vitronectin has a similar functionality regardless of the wettability of the surface; however, it can adhere better to hydrophilic surfaces. In particular, highly hydrophobic surfaces adsorb hydrophobic proteins/protein motifs and vice versa. This, in turn, affects the cell or tissue response [36]. Topography may also affect surface protein adsorption in several ways. The increase in surface area may increase total adsorbed protein content. Moreover, confined spaces in the topographic features may interfere with wetting and protein adsorption on the surface [35]. All these effects on protein adsorption will determine the cell response. For example, nanotopography was found to affect

protein adsorption on polymeric substrates; decreased adsorption resulted in lower proliferation and rounded morphology in fibroblasts [37]. Fibronectin adsorption and accordingly endothelial cell adhesion and proliferation was altered in silica surfaces coated with 21 nm colloidal silica nanoparticles, compared to uncoated silica surface. It was suggested that fibronectin conformation may have been changed on the particles, therefore reducing the number of cell-binding fibronectin domains presented to cells. [38].

Roughness is known to affect cell adhesion; however, different results have been achieved for different cells and materials. The exact relationship between the substrate roughness and cell adhesion is not known. However, models are available. For example, it has been suggested that the effect of roughness on cell adhesion is a function of the surface energy, which is related to the adhesion strength of the cells to the substrate. As such, surface energy depends on the material and coatings applied. For small surface energy (substrates to which cells cannot adhere very well), roughness would further decrease cell adhesion. For intermediate surface energies, roughness would be irrelevant for cell adhesion. Finally, for large surface energies, roughness could have a beneficial effect, and an optimal roughness could be found which maximizes cell adhesion. [39]

1.3 Light-Matter Interactions and Surface Structuring

The various applications of lasers in biology can be broadly categorized into bio-micro-device fabrications and tissue engineering applications. Some specific areas include biomaterial laser printing, DNA or protein microarrays, cell printing, selective laser sintering, various forms of lithography and near field processing techniques [40]. Laser structuring of materials may result in a wide variety of structures, depending on various laser, material and structuring parameters. A thorough understanding of the underlying processes can allow the prediction of the topographies resulting from the chosen parameters.

1.3.1 The nature of light

Light has been established in the quantum mechanical theory as having both wave and particle nature. In particular, the wave nature of light is appropriate when discussing light propagation until the surface of the material to be irradiated, while the particle nature becomes more relevant once the light interaction with the material starts to take place. As such, both views will be useful in building the theory on the light-substrate interactions which lead to the topographies used.

The wave theory describes light as an electromagnetic wave with sinusoidally varying electric and magnetic fields. Their directions are such that their cross product (E x B) gives the direction of propagation. The behavior of these field components at any given time during the light propagation or at boundaries can be described using the well-established Maxwell's equations. The polarization of light refers to the direction of the electric field, and is important in the light behavior at boundaries, as well as in the formation of specific periodic surface topographies.

As a wave, light has wavelength (λ, unit m) and frequency (ν unit s^{-1} or Hz), which are related to each other by the following equation:

$$c = \nu\lambda$$

where c (unit m/s) is the speed of light. The energy carried by the light is dependent on its wavelength, with longer wavelength waves carrying less energy. At boundaries, part of the light will be reflected while the rest will be transmitted into the new medium. This fraction of transmitted light is given by Fresnel's equations, which are derived by solving the wave equations with the appropriate boundary conditions. The reflectivity depends on the material's properties, the environment, the angle of incidence, the wavelength and the polarization of the light beam. For normal incidence, the Fresnel Equation below is valid for both polarizations, perpendicular and parallel to the plane of incidence:

$$R = \left(\frac{n_1 - n_2}{n_1 + n_2}\right)^2$$

The reflectivity further depends on the light's wavelength, temperature, as well as local plasmonic effects [41, 42]. The portion of light which is not reflected will be transmitted through the material and may be absorbed. In absorption phenomena, the particle nature of light becomes more appropriate.

Particles of light are called photons. Each photon carries an energy is related to the frequency (or wavelength) of light by Planck's constant, h $(6.62 \times 10^{-34}\mathrm{m}^2\mathrm{kg/s})$, by the following equation:

$$E_{photon} = h\nu = \frac{hc}{\lambda}$$

During the absorption process, the energy of the photons is transferred to the electrons in the material, promoting them to excited states. The energy required to promote the electrons of the material to an excited state depends on the material's properties. Note the formula gives the energy in Joules; it can be converted to electron volts (eV) by using the following conversion: $1\mathrm{J} = 6.24 \times 10^{18}\mathrm{eV}$.

1.3.2 Properties of silicon

The interactions of the light of chosen wavelength with the chosen material are important in understanding the processes involved and the final topography results. Relevant information about the silicon material is summarized below.

Silicon is the second most abundant element in the Earth's crust. Its atomic number is 14, and it is a semiconductor. Crystalline silicon has a diamond lattice unit cell. In the crystal, each Si atom forms 4 covalent bonds with neighboring atoms, forming a tetrahedral structure. The crystal structure of silicon and the three planes formed by its lattice are of special interest in some silicon microfabrication techniques, such as etching. Crystalline silicon can be obtained from its source material (sand, quartzite rock) using well-established methods, such as the Czochralski Method or the Float

Zone method. For the fabrication of microelectronics, silicon may be doped with either phosphorus (N-doped) or boron (P-doped). The crystalline silicon is sliced into disks called *wafers* and may be further polished. Wafers come in different shapes (round or semi-squared), sizes, thicknesses (279 μm or 525 μm), and they may be polished at one (single side polished) or both sides (double side polished), or non-polished (*as-cut*). When in contact with air, an oxide layer a few nm thick is present at the silicon's surface [4].

The electronic states of silicon are similar to those of other semiconductors. Quantum theory has established that in an atom, electrons may only have discrete energetic states, with no more than two electrons allowed to have the exact same energy (Pauli exclusion principle). This principle also holds true for more than one atom: when two atoms are close enough to interact, their electrons also have to be in separate energy states. This causes the energy levels to split and form *energy bands*. These are composed of a large number of energy levels, which are closely spaced together and resemble a continuous band. Semiconductors have characteristics electronic band structures, with a *valence band* (the highest energy band which is filled) and a *conduction band* (the band above the valence band). Electrons may be found in the valence band (when in ground state) or in the conduction band (when in excited state), but not between them. The energy difference between the top of the valence band and the bottom of the conduction band is referred to as the *band gap*. No electronic states are allowed in the band gap; for this reason, an electron needs to absorb an energy which is equal or greater to the band gap energy in order to be promoted to the conduction band. For silicon, the bandgap energy is 1.12 eV. An electron may be excited by a single photon of energy 1.12 eV or greater, or by two-photon absorption of lower energy photons. When an electron is promoted to the conduction band, it leaves an empty spot called a *hole*. Once an electron is in the conduction state, it is free to move around the lattice with any kinetic energy it has; similarly, the hole may also move up to the top of the valence band. Eventually, the two recombine non radiatively.

Silicon's optical properties, such as reflectivity and absorbance at different wavelengths, have been studied in detail. The reflectivity of silicon is shown in the Figure 1.3 below. For the wavelength used in this work (1030 nm) it can be extrapolated from the graph that the reflectivity is around 0.3.

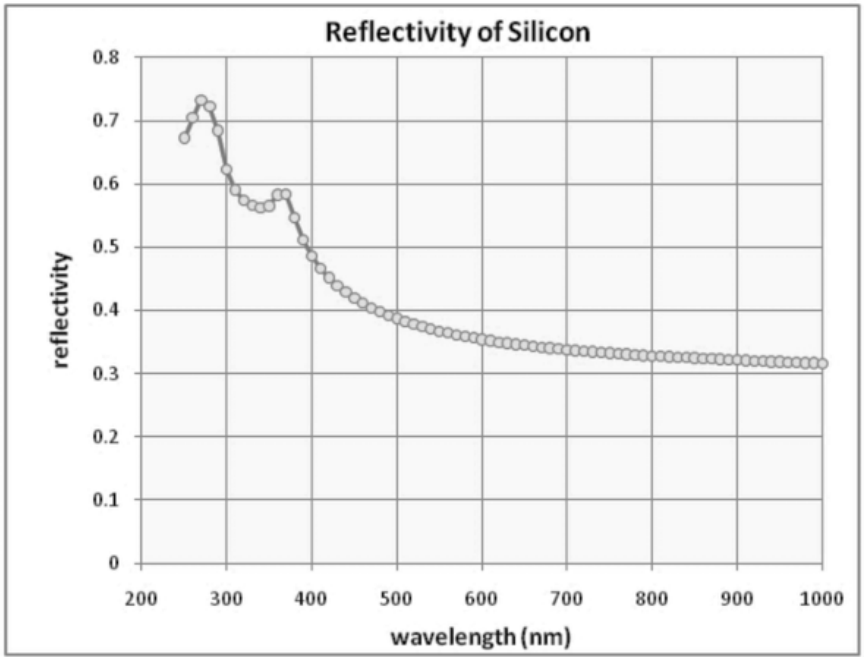

Figure 1.3: Reflectivity vs. wavelength for silicon, adapted from pveducation.org

Due to light's interaction with the material, the light intensity decays with depth, as described by the Beer-Lambert law:

$$I(z) = I_0 e^{-\alpha z}$$

For 1030 nm, the absorption coefficient α for silicon is reported as 30.2 cm^{-1} [43]. This value can be used to calculate the depth at which the intensity will have fallen to 1/e (37%) of its original value as 330 μm. This depth may be valid for one photon absorption processes; however, it can be affected by other factors, such as two-photon absorption, temperature, pulse length and local plasmonic effects [41, 42]. For short laser pulses, the entire optical energy is absorbed at the surface [44]. As energy is absorbed by the material, different thermal processes such as melting, amorphization, annealing, boiling or explosive boiling may take place at the surface, depending on the amount of energy deposited on the material. For silicon, the modification threshold was reported as 0.26 J/cm2; larger energies may result in loss of crystal structure (amorphization). On the other hand, energies larger than 0.55 J/cm2 lead to annealing [4]. Even higher energies are needed for boiling.

1.3.3 Laser properties and operation

Lasers (acronym for Light Amplification by Stimulated Emission of Radiation) are powerful sources of highly coherent light. Lasers typically deliver highly coherent light with narrow spectral width. There are various types of lasers, changing in many different parameters. One particular parameter is whether the light is delivered continuously (continuous wave, or CW lasers) or in pulses, with the laser being on and off for certain amounts of time (pulsed lasers). The duration of laser pulses can be as short as a few femtoseconds, with each pulse delivering vast amounts of energies. For pulsed lasers, pulse length and repetition rate (in pulses/second) are of importance in the structuring of materials. Laser systems used for material processing usually also contain motorized precision stages, Galvo heads for scanning the laser beam, a variety of optical elements to control the beam (mirrors, collimators, focusing lenses, amplifiers...), power meter, as well as appropriate software to control the stages and the scanning design.

The laser used in this study was a femtosecond laser system, with the properties summarized in the Table 1.1 below:

Table 1.1: Properties of the ultrafast laser used in this study

Central wavelength	1030 nm
Repetition rate	1 MHz
Pulse duration	370 fs
Average power	360 mW
Spot size	9 μm
Scanning velocities	Up to 3000 mm/s

From this table it is understandable that the laser is on for 370 femtoseconds every 10^{-6} seconds, so it is on for a very short time, with 10^6 repetitions every second. The average power is the total power measured in one second. For material structuring purposes, the energy delivered in one pulse is more relevant. It can be calculated from the average power by using the following relations:

$$\text{Power } (W) = \frac{\text{Energy } (J)}{\text{time } (s)}$$
$$\frac{\text{Energy}}{\text{pulse}}(J) = \frac{\text{Energy/second } (J)}{\text{Pulses } / \text{second}}$$

Plugging in, we get, for 360 mW power:

$$\text{Energy/pulse } = 3.6 \times 10^{-7}\text{J}$$

However, due to the short duration of each pulse, the intensity for each pulse is quite large:

$$\text{Intensity} = \frac{\text{Power}}{\text{Area}} = \frac{\text{Energy}}{\text{Time} \times \text{Area}}\,(W/cm^2)$$
$$\text{Intensity} = \frac{3.6\times10^{-7}J}{370\times10^{-15}s\times\pi\times(9\times10^{-4}\text{cm})^2}$$
$$\approx 3.8 \times 10^{11}\text{W/cm}^2$$

The laser is raster scanned on the surface; the shape may be designed in the accompanying software. A simple raster scan is shown in Figure 1.4:

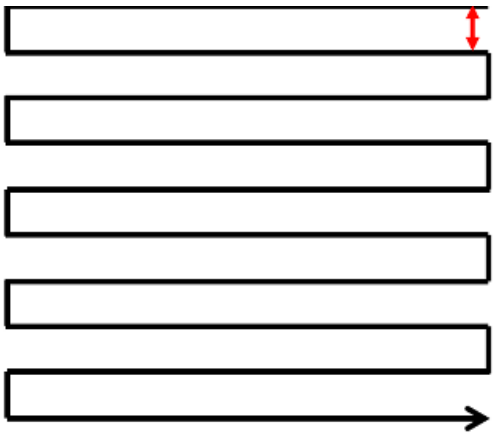

Figure 1.4: Raster scan diagram used for laser structuring

In the figure, the red arrow represents the constant distance between each two raster scan lines. The distance between the lines is called *hatch*. It is obvious that the laser

velocity and fluence will influence the effective number of laser shots which will fall at a particular spot. One can start by considering a single line. The laser velocity considered can be the maximal scan speed (3000 mm/s = 3 m/s). The spot size is 9 μm and the repetition rate is 1 MHz, corresponding to 10^6 repetitions every second. The number of pulses per spot (N) for this velocity is:

$$N = \frac{\text{Total length of structured area}}{\text{Total travelled distance for the beam}}$$

$$= \frac{\text{Repetition rate} \times \text{Time} \times \text{Spot diameter}}{\text{Velocity} \times \text{Time}}$$

$$= \frac{\text{Repetition rate} \times \text{Spot diameter}}{\text{Velocity}}$$

$$N = \frac{10^6 \text{pulses/s} \times 9 \times 10^{-6} \text{m/pulse}}{3 \text{m/s}} = 3 \text{ pulses/spot}$$

The slower the laser goes; the more pulses can be delivered to a single spot. A schematic representation of the affected area for three different velocities is shown in Figure 1.5 below.

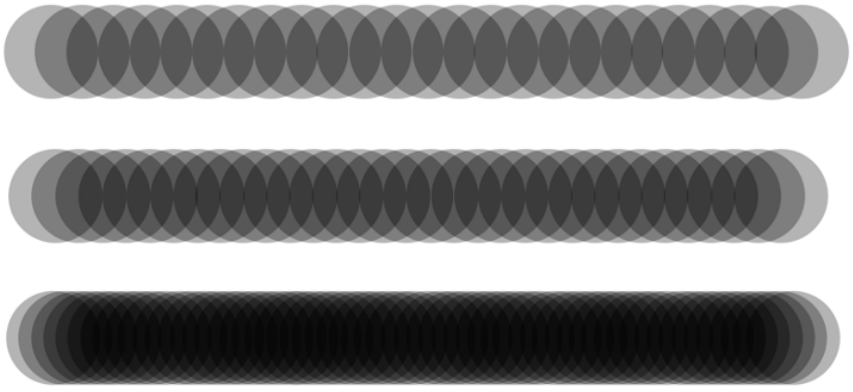

Figure 1.5: Schematic representation of laser spots overlap for different velocities

For lower hatch values, overlap between the two raster scan lines is also possible (for values smaller than 9μm), effectively increasing N for a given spot and hence the total

energy hitting any spot (besides the corners). A schematic diagram is shown in Figure 1.6 below.

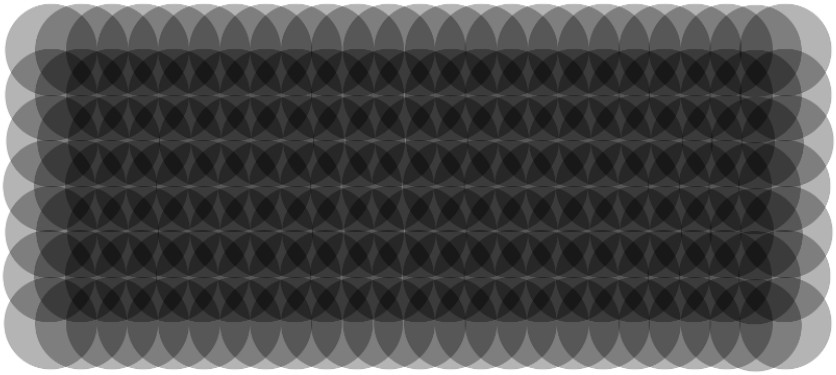

Figure 1.6: Schematic representation of affected areas showing overlap between two scan lines for low hatch values (H < 9 μm).

1.3.4 Processes involved in laser-substrate interactions

A theoretical background on the general mechanisms of laser interaction with materials may be found in the literature [3, 44, 4]. A diagram representing the four major steps of the process, together with their timescales is shown in Figure 1.7 below. Note that in this study, the next pulse begins at 10^{-6} seconds.

The first step of the process, carrier excitation, is the absorption of irradiation by the carriers in the material. For silicon, single photons with energy greater than the bandgap (1.12 eV) are able to excite electrons to the conduction band. The process involves a phonon due to the indirect band structure of silicon. As electrons are promoted to the conduction band, the band structure changes; the band gap decreases until it eventually collapses, when a certain percentage of electrons are in the conduction band. Promotion of more electrons to the conduction band may occur through impact ionization, where electrons with enough kinetic energy excite other electrons through collisions. This way, the absorbed optical energy is transferred to the carriers as excitation to the conduction band and kinetic energy. During thermalization, this energy is redistributed through carrier-carrier or carrier-phonon scattering. In carrier-carrier scattering, the carriers interact with one another until they reach a Fermi-Dirac dis-

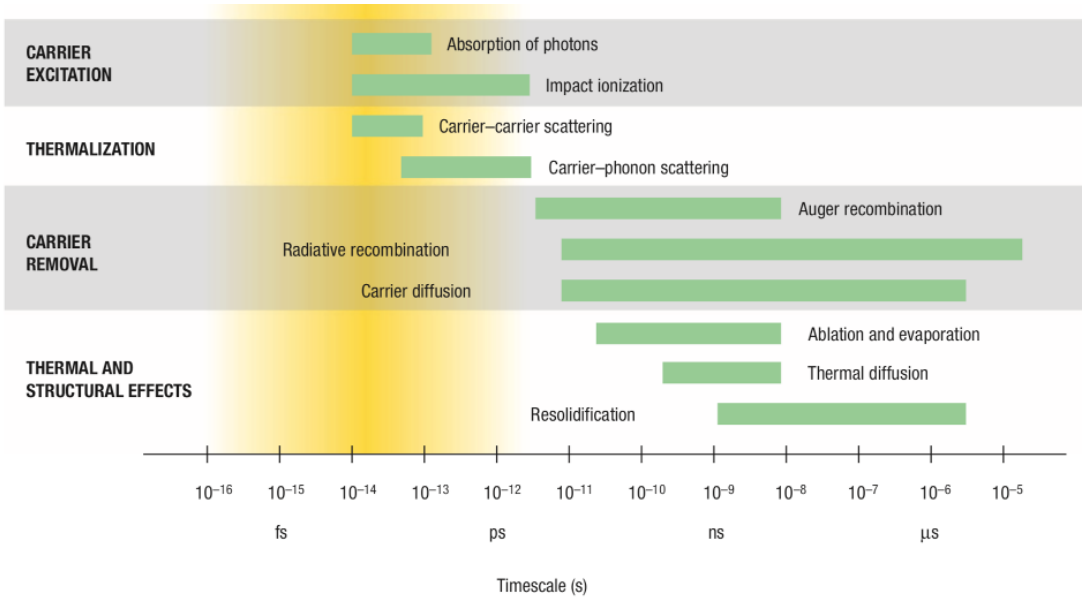

Figure 1.7: Timescales of different events taking place during laser structuring of materials. Adapted from [3].

tribution after some hundreds of femtoseconds. On the other hand, in carrier-phonon scattering, energy is transferred to the lattice. This process occurs through phonons and it takes several picoseconds for the carriers and the lattice to reach thermal equilibrium. In this point, the carriers and lattice will have the same temperature. After this thermal equilibrium is reached, any excess carriers are removed through different mechanisms. Excess carrier removal may take place through recombination events, where electrons fall to the ground state and *recombine* with the holes, releasing energy. Recombination may be radiative or non-radiative, with each particular recombination channel having its own probability which is dependent on the material. In radiative recombination, a photon is released as excess energy; however, such a radiative decay is not allowed in silicon due to silicon's indirect bandgap. Instead, non-radiative decay processes are preferred in this material. Examples of non-radiative decay processes are trap states (not shown in the Figure 1.7) and Auger recombination. In Auger recombination, the excess energy from electron-hole recombination is transferred as kinetic energy to another conduction band electron. Finally, the excess carriers may also be removed from a region through carrier diffusion, however, this process depends on the pulse duration of the laser and is generally slower on ultrafast lasers. In any case, after thermal equilibrium is reached and excess carriers have been

removed, the effects on the material resemble any other type of heating. Phase transitions (melting, evaporation) may occur if the respective temperature thresholds have been reached. Simultaneously, non-thermal effects may also occur in materials irradiated with laser pulses of picosecond or sub-picosecond duration [3]. The *non-thermal plasma model* describes lattice disordering through direct excitation of the electronic system. According to this model, the atoms gain mobility without thermal energy increase when about 10% of the valence electrons are promoted to the conduction band. In another reference, this is termed as *bond softening* [4].

The thermal and structural effects depend on the energy deposited onto the material, or laser fluence (measured in J/cm^2). As described previously, the optical energy is absorbed by the electrons and transferred to the lattice; this may cause phase changes such as melting, boiling or ablation. The different structural effects taking place in silicon upon irradiation with femtosecond laser pulses are shown in Figure 1.8. A Gaussian beam is assumed in Figure 1.8, with the center of the irradiated spot receiving the highest fluence as shown in the graph.

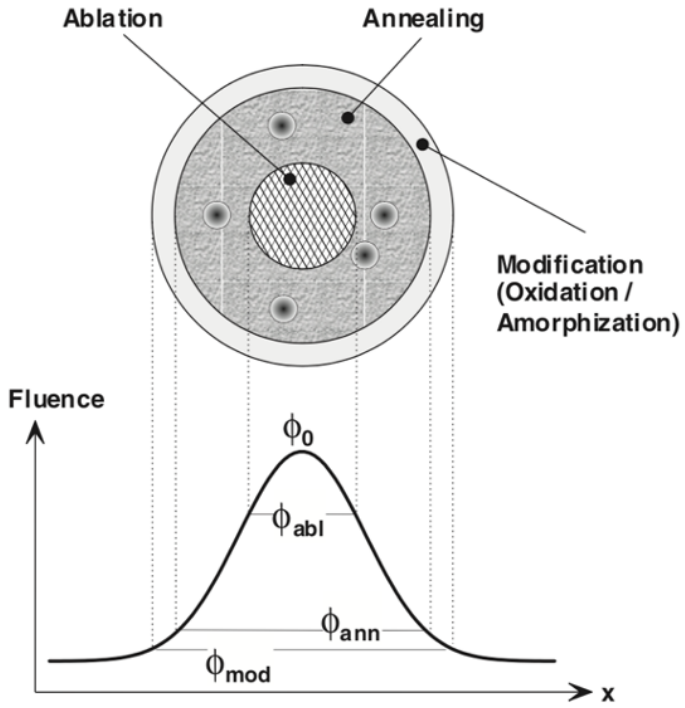

Figure 1.8: Physical processes during the modification of silicon with femtosecond laser pulses [4]

Modification occurs at the lowest fluences and refers to oxidation and amorphization processes. In oxidation, silicon reacts with the oxygen in the air to form oxides. In amorphization, the crystal structure is lost. The oxidation regime has particular importance in the formation of a highly regular periodic topography in other materials [45]. Oxidation of the formed structures takes place due to the laser structuring of Si in ambient atmosphere, forming silica structures [46]. Annealing, on the other hand, occurs at higher fluences. Annealing is a process commonly used for silicon wafer doping. During this process, silicon re-solidifies in a crystalline form. The reason for the difference in solidification between modification and annealing is cooling rate. Lower temperatures (in modification) do not allow for slow cooling rates and silicon is solidified in amorphous state. If the material had come to a high enough temperature, on the other hand, cooling is slow and re-crystallization happens. Finally, ablation refers to removal of material (molecules, clusters, nanoparticles) from the material's surface. Ablation requires relatively high fluences, as it can be seen in Figure 1.9. In the process of ablation, rapid melting at the surface layer causes a pressure gradient and a tensile wave, resulting in void nucleation inside the liquid layer. These voids then coalesce and cause material expulsion. In regions with higher fluence, temperature is higher and cooling rate slower, therefore the bubbles may grow even larger and yield to more material ablation [4]. Ablation is important in the formation of different types of surface structures, including some subtypes of periodic surface structures [47].

Figure 1.9 summarizes the different processes resulting in different topographies. They are oxidation, amorphization, re-crystallization, bubble formation due to subsurface boiling and ablation [4]. Ripples and columns are among the resulting topographies.

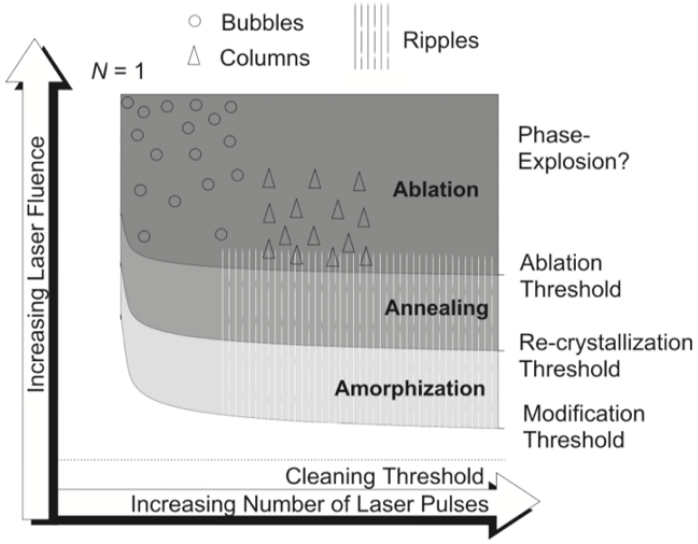

Figure 1.9: Morphological phenomena after irradiation of the silicon surface with linearly polarized light of 100 fs duration. Reproduced from [4]

1.3.5 Theories behind the formation of LIPSS and Microcolumns

The two main considered topographies are laser-induced periodic surface structures (LIPSS) and Microcolumns. Both types of structures have been described previously, and the parameters under which they form, as well as theories behind their formation, are known.

LIPSS, also called *ripples*, are a surface relief composed of quasi-periodic or periodic lines. These ripples form when a linearly polarized laser beam is scanned on the surface. Since their discovery in 1965, there has been an increase in the number of papers published on LIPSS theory or applications [48]. There are various types of LIPSS. They may be classified according to wavelength; in which case we can differentiate low-spatial-frequency LIPSS (LSFL) with periodicity similar to the laser's wavelength; and high-spatial-frequency LIPSS (HSFL) with periodicity smaller than half the laser's wavelength. They can also be referred to as coarse and fine ripples, respectively [49]. LIPSS may also be classified according to their orientation as either parallel or perpendicular to the polarization of the incident light. When perpendicular to the laser polarization, the structures are called *normal* LIPSS, while those parallel to the polarization may be called *anomalous* LIPSS [47]. LIPSS may be

generated using a wide range of laser pulse lengths; for ultrafast (femtosecond laser) pulses, LIPSS are covered with nano-sized features such as nanoparticles, nanorods and nanocavities with sizes as low as 20 nm [50].

Theories on LIPSS formation are available in the literature [51, 4, 48, 47]. It is generally accepted that LIPSS ripples start to form due to the interference of incident light with the surface plasmon polariton wave after scattering on any surface defect, such as asperities or scratches, and that feedback mechanisms are involved [52, 45, 4, 47]. Surface plasmon polaritons (SPPs) are electromagnetic fields which propagate at the interface between a metal and a dielectric. They are oscillations of the surface electrons and may happen due to the coupling of incident photons. SPP waves propagate while decaying. A SPP mode may be excited through surface roughness and discontinuities, which provide the conditions for momentum matching processes which can couple the SPP to the surface. The idea that LIPSS originate from the interference of incident light with surface plasmon polaritons was put forward by Keilmann and Bai [53], whereas Sipe *et al.* coined the term *LIPSS* and developed a first-principle theory on the formation of the structure [54]. They introduced an "efficacy factor" which described the interactions of the incident light with a rough surface. This theory is still valid, but it does not describe all types of LIPSS. The combination of Sipe's theory with a Drude model (which describes the behavior of carriers in a material system) was successful in describing the formation of LIPSS on silicon and emphasized the importance of permittivity changes during material irradiation with ultrafast laser pulses [51]. Silicon, and generally semiconductors, are initially non-active plasmonically. However, changes in electronic band structure following the promotion of a large number of electrons into the conduction band turns these materials into metallic, and the excitation of the surface plasmon polaritons becomes possible. The SPP interferes with the incident light; therefore, light will be preferentially absorbed in particular regions of the surface.

The fluence determines the structural changes which take place in the regions of absorption. Normal LIPSS is a result of ablation while anomalous LIPSS is due to oxidation. In both cases, the incident light interference with the surface waves scattered from surface defects leads to inhomogeneous oxidation or ablation. Analysis of LIPSS resulting from different irradiation conditions is usually implemented in

order to shed light on the processes underlying the LIPSS formation. It is possible to generate normal or anomalous LIPSS by changing the fluence and repetition rate. For normal LIPSS, high fluence and low pulse number (several pulses) are used; whereas anomalous LIPSS requires lower fluence and higher pulse number (several thousand pulses) [47]. One study analyzed the cross section of the ripples with SEM, and the authors drew some conclusion on the formation mechanism based on the cross-sectional features. Coarse ripples were shown to be convex with narrow valleys (grooves). It was suggested that this was due to the phase transformations; amorphization in coarse ripples causes volume expansion which makes the ripples more convex [49].

Several feedback mechanisms are involved in the formation of LIPSS. It was mentioned that LIPSS start out by the interference effect on surface defects. As LIPSS form, the surface topography changes and the formed structures can serve as scattering points for the next pulse [45, 48]. This feedback effect can be exploited to make large-area regular ripples by overlapping the irradiation spots. The surface optical properties at each pulse depend on the surface topography at the beginning of the pulse, as well as the variations in the dielectric function of the surface which occur due to the laser irradiation during the pulse. This is formalized in one study, where an equation describing the feedback process was proposed. Positive sign feedback favors the formation of periodic, ordered ripples while negative sign feedback results in random surface roughness. It was suggested that after a preliminary LIPSS structure is formed, then the feedback function changes sign leading to roughness. After more shots, the feedback changes sign again and a secondary LIPSS is formed, which is then not subject to more change [55]. This prevalence of the LIPSS structure after its formation is also described for oxidation-type LIPSS as a *"negative feedback"*effect, where the limit of oxygen diffusion prevents any further growth or change of the structures and excess laser shots exert no further change on the topography [45, 47]. On the other hand, ablation type LIPSS does not have any inherent feedback, excess laser shots eventually result in LIPSS destruction, therefore the anomalous LIPSS may form only with a certain range of shots (hence, a certain range of laser scan velocities) [47]. Furthermore, the surface electromagnetic wave (SEW) propagation limits the LIPSS regularity. The decay length (or mean free path) of the excited SEW

depends on the material. Materials such as Mo, Ti and steel, which have high optical losses at the irradiation wavelength and short SEW decay lengths, can support highly regular LIPSS. On the other hand, materials with long SEW decay lengths allow for more unwanted interactions of the SPP with itself or other surface irregularities, and result in less regular LIPSS with bifurcations and discontinuities [56].

For fluences above threshold (which initially result in ablation-type LIPSS) as the number of pulses increases, micro-column topographies start to form. After ripple formation, the surface acquires topographical features which change the angle of incidence of the laser light at each point. Light is further guided by reflections on the various surface features. The most absorption takes place at the topography maxima or minima. As the material vaporizes with increasing number of pulses, the vapor is preferentially deposited at the top parts of the topography, forming growing structures [4]. The structures have column-like or hill-like shape of micron-scale height. The microcolumns may be covered with LIPSS, by scanning the laser beam on the microcolumn topography with an adequate velocity to obtain LIPSS [52].

Although polymers cannot be easily structured with laser, LIPSS topography can be transferred efficiently and reliably to various polymer biomaterials. This increases the range of materials on which the effect of LIPSS on cells can be studied [57]. Due to changes in surface roughness, the wettability of the surface changes after laser processing. For example, LIPSS-covered surfaces show higher hydrophobicity; this is thought to be caused by the trapping of air underneath the liquid, in between the nano-scale surface topographies of LIPSS [48].

1.4 Cell-substrate interaction studies involving femtosecond laser structuring, LIPSS, or silicon

The effect of femtosecond laser treatment of different materials on cell response has been studied for various cell types. For example, femtosecond laser treatment of silicon has been used to produce inhibitory regions for HeLa cells [46]. Femtosecond structuring of stainless-steel stents, producing micro-structures with secondary nanostructures, was shown to decrease the proliferation of monocytes. Endothelial

cell proliferation was not affected. As such, femtosecond laser treatment of stents was proposed as an appropriate modification to increase stent function [58]. On stainless-steel plates, femtosecond laser structuring was shown to improve the surface's hydrophilicity and increase its carbon content. Laser-treated surfaces significantly improved the adhesion of endothelial and bone marrow mesenchymal cells, while decreasing the adhesion of fibroblasts. In this aspect, this surface modification was proposed as appropriate for bone prostheses [59]. Femtosecond laser treatment was used in one study to fabricate different structures on stainless steel, such as 2D periodic grating, pseudo-periodic coral-like structures and 1D grating (channel-like) structures. The structures were also reliably imprinted onto polycarbonate. Cell alignment was observed on the 1D gratings, whereas corals were shown to inhibit cell proliferation [60]. Femtosecond laser irradiation of polydimethylsiloxane (PDMS) changes the topography and wetting properties of the material and allows for the fabrication of hydrophilic and superhydrophobic regions on the substrate. This effect was used to control the adhesion of C2C12 cells and achieve cell patterning [61]. Femtosecond laser structuring of Ti was used in conjunction with aerosol beam irradiation to produce periodic structures of 230 nm periodicity and 150 nm height. Osteoblasts showed alignment in the direction of the nanostructures.

In several studies, LIPSS topography was achieved and its effects on different cell lines were studied. Structuring of polystyrene (PS) with a 248 nm linearly polarized laser beam at different angles produced periodic structures of periodicities 200-430 nm and depths 20-100 nm. Cell experiments showed that HEK293 cell proliferation increased on the structured PS, whereas CHO-K1 cells and skeletal myoblasts aligned to the periodic structures. The periodicity which elicited maximal cell alignment was cell type-specific [62]. LIPSS topography on Ti-6Al-4V was found to enhance matrix mineralization in hMSCs cultured in osteogenic medium [63]. LIPSS texturing of stents increased adhesion of fibroblast cells while inhibiting monocyte attachment, both features important for stent functionality [64]. In one study, LIPSS was combined with micrometer-scale gratings in a "double contact guidance", to see which scale topographical cues had more effects on the cells. It was found that cells initially interact with the LIPSS topography, but later align to the micrometer-scale gratings [65]. LIPSS topography with a period of 600 nm and depth 100 nm was formed on

polyethylene terephthalate (PET) surface by direct structuring with a femtosecond laser. MG-63 cells showed spreading along the LIPSS grooves [66]. LIPSS with various periodicities (300-400 nm) and average roughness values (Ra = 37-42 nm) were formed on polymers using femtosecond laser irradiation at different angles. Myoblasts cultured on these substrates showed alignment in the LIPSS direction; as well as changes in the localization of beta-catenin and VE-cadherin proteins. [67]. Micro-column topographies have also been considered. Some micro-columnar structures have been found to increase cell adhesion [68], while others inhibited cell growth [60]. Femtosecond structuring of silicon was used to fabricate areas with micro-spike and micro-column topographies. These topographies had different average roughness values. As laser fluence increased, spike sharpness and hydrophobicity also increased while fibroblast proliferation and survival decreased. However, thermal oxidation of superhydrophobic surfaces increased their hydrophilicity as well as the ability of fibroblasts to adhere to them. [36].

Silicon was chosen as the base material in this study due to its availability, the ease of structuring with ultrafast laser, and the large amount of structures which can form on this material. Although not a common implant material, silicon is used in some brain electrodes. Furthermore, due to the large amount of modifications possible on silicon, many studies have used this material as a cell culture substrate, and the effects of different silicon modifications on specific cell types have been reported. For example, when grown on various etched silicon substrates, nigral cells were shown to preferentially adhere to surfaces with average roughness Ra from 20 to 50 nm [69]. Porous silicon was found to increase proliferation in N2A cells and immortalized human cortical neuronal cells (HCN1A), compared to flat silicon [70]. One group generated randomly rough silicon substrates with defined average roughness Ra and fractal dimension, in order to study cell behavior. Fibroblasts were studied as model cells; proliferation was increased in roughness Ra of 40 nm and fractal dimension (Df) 2.4, while adhesion was favored on Ra values of 50 nm and Df of 2.2 [71]. Silicon substrates with various size pillars generated through lithography was used with neural cells in a time-lapse study to discern the effect of the nanotopography on the first neurite budding. It was found that the topographical cues attracted N-cadherin and the first bud was oriented towards the pillars [72]. Stereo-topographical

nanowires (SiNW) were formed on silicon by an electroless metal deposition method, which produced nanowires with controlled length and orientation. This topography was shown to negatively affect the growth of human mesenchymal stem cells, causing spherical cell shape and loss of viability. SiNW length was found to affect the expression of COL1A1, Runx2 genes, as well as the levels of F-actin, phosphorylated FAK, vinculin and alpha 2 integrin, suggesting osteogenic differentiation control through cytoskeletal remodeling [73]. The effect of porous silicon with different pore sizes was studied on one substrate following asymmetric electrode anodization to produce pore gradients. It was found that large pore sizes (>100 nm) negatively influenced adhesion of SK-N-SH neuroblastoma cells. Pores less than 50 nm, on the other hand, positively influenced cell adhesion and allowed for the development of processes [74]. "Wave-ordered structures" of various pitches, ridge widths and depths were formed on silicon using a lithography-free ion beam process. Human corneal epithelial cells (HCEC) aligned best to a topography which overlaid two different WOS patterns, 200 nm depth and 70 nm pitch topography on 4000 nm pitch, 400 nm deep topography. The authors hypothesize that there is a minimum depth that cells will align to; for HCEC it was found to be similar to the range of cornea fiber dimensions (20-90 nm). However, the smallest dimensions that a cell would respond to seem to be highly dependent on cell type [75]. The effect of roughness on neural cell growth was studied by etching silicon substrates for different times. It was found that neurons grow and survive for over 5 days on substrates with average roughness of 20-70 nm [69]. Finally, although it is not a common implant biomaterial, silicon is being used in implanted "next generation" electrodes, due to the flexibility it offers in electrode design. Given the large amount of modifications possible on silicon, it may be possible to optimize the electrodes for neural cell survival and for the minimization of glial scar tissue formation. [76]. Although one cited study had concluded that the surface topography of silicon does not affect scar formation, only two topographies were considered (smooth and rough).

1.5 Aim of the thesis

The aim of this study is to observe the behaviors and responses of Neuro-2a cells on femtosecond-laser structured silicon substrates.

Neuro-2a cells have not been previously studied on silicon substrates structured with femtosecond lasers. These cells are important models of neural cells and have been previously shown to be affected by substrate topography on other materials. Silicon was shown to be an appropriate cell culture substrate for Neuro-2a cells as well as other cells. On the other hand, laser structuring was shown to alter cell behavior in many different cells and various materials including silicon. The aim of this thesis is to observe if the laser structuring of silicon has any effect on Neuro-2A cell behaviors.

For this purpose, different silicon substrates were structured, characterized and prepared for cell culture. Meanwhile, fluorescent constructs targeting the cell membrane, nucleus or actin cytoskeleton were used or prepared as needed. Cells were transfected with different fluorescent constructs and grown on these substrates for different amount of times. Observation of cells was done with fluorescence microscopy of either live or fixed cells, or SEM. Possible changes in cell motility and exploration behavior, shape, alignment, number, as well as fine details of the cell adhesion were noted.

CHAPTER 2

MATERIALS AND METHODS

2.1 Substrate preparation and characterization

2.1.1 Silicon wafer, cutting and handling

Single side polished, CZ, p-type monocrystalline silicon wafers of thickness 525 μm were used. Wafers were cut into squares of side 5 mm, 10 mm or 16 mm depending on the experiment. The 16 mm ones were used for live imaging experiments, because they can stay upside down onto glass bottom dishes in a stable way with minimal surface loss. The 5 mm and 10 mm substrates were used for imaging of fixed samples, since the small surface area allowed for fast imaging of the whole sample. The samples were kept in closed containers until laser structuring.

2.1.2 Laser structuring

Laser structuring was carried out in air and room temperature, using a home-made ultrafast laser. All procedures were carried out in accordance with the safety rules of Class 4 lasers. The laser had a central wavelength of 1030 nm, pulse length 370 femtoseconds, repetition rate 1 MHz and the average power used was 650 mW. The focused beam spot size was 9 μm. The laser setup is represented schematically in Figure 2.1.

The laser system was equipped with a precision motion stage for stage control, a Galvo head for beam scanning as well as half wave plate for polarization control. A photo of the setup is shown in Figure 2.2. The beam passes through the various optical

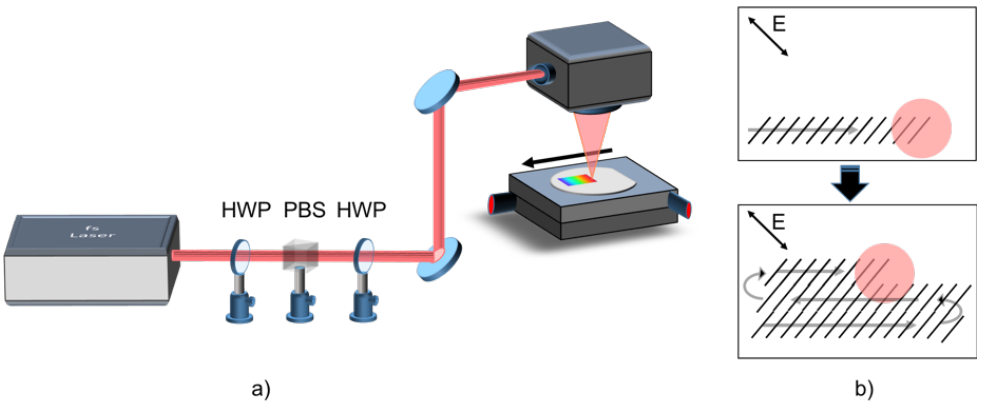

Figure 2.1: Schematic representation of the laser used in this study. Adapted from Pavlov et al. [45]

elements before being focused on the sample, which is placed on the 3D stage. The polarization can be controlled using the polarizer shown in the Figure. The power can be adjusted and measured with the powermeter.

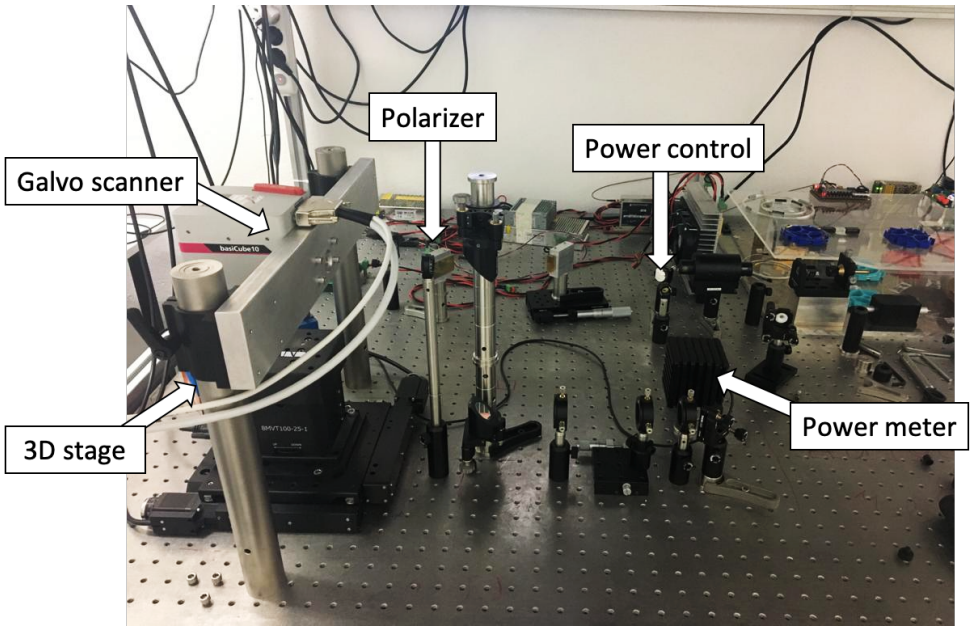

Figure 2.2: Photo of the laser and structuring setup, showing the Galvo scanner, 3D stage, power meter and other optical elements.

The system was was operated using Standa and SamLight software. The software allowed the full design of the structuring. The major shape was drawn (square) and the dimensions were determined (usually several mm; different sizes were used in

different experiments). The raster scan mode was selected, the scan velocity was determined, and the hatch value was determined. For whole-area structuring, the hatch value used was 4.5 μm. For line topographies, larger hatch values such as 40 μm were used. Overlay of topographies was possible by drawing a second major shape, selecting the appropriate hatch and scan velocity and centering it with the first one. The silicon substrates were placed onto the stage using tweezers and the focus position of the beam was determined manually. After the focus was found, the structuring was carried out according to the design. At least four replicas were done for each substrate.

2.1.3 Substrate cleaning

After processing, the substrates were cleaned using 3 solvent cleaning (acetone, absolute ethanol and isopropanol for 10 minutes each in ultrasonic bath) and dried using nitrogen air flow. One of the replicas was used for substrate characterization while the other three were stored in closed containers for cell culture experiments.

2.1.4 Surface characterization

Atomic Force Microscopy (AFM) measurements were carried out using a Nanomagnetics Instruments Ambient AFM in dynamic mode, for LIPSS and microcolumn substrates. Scanning Electron Microscopy (SEM) measurements were carried out using a Zeiss SEM, for all topographies. The topography images were analyzed using Gwyddion software.

2.2 Preparation of LifeAct-EGFP

The cells were transfected with fluorescent proteins such as Enhanced Green Fluorescent Protein (EGFP) or mCherry in order to make them visible in the inverted microscope. This was due to the opacity of the silicon substrates. The DNA constructs were actin marker LifeAct-EGFP, nucleus-localized NLS-mCherry and membrane-localized Gap43-EGFP. These constructs allowed the visualization of f-actin, the

nucleus and the plasma membrane, respectively. Out of these, NLS-mCherry and Gap43-EGFP were available, while LifeAct-EGFP was prepared for this thesis work. LifeAct-EGFP was prepared for the present work according to the sequence available in [77] .The construct was prepared using standard molecular cloning techniques.

2.2.1 Reaction and primer design

The LifeAct sequence together with the linker was obtained using polymerase chain reaction (PCR), as double-stranded DNA containing the desired sequences flanked by appropriate restriction enzyme cleavage sites (XbaI and EcoRI) and an additional flanking sequence *GTTGTTGTT* at both the 5' and 3' end to allow for proper restriction digestion. The LifeAct sequence was subsequently inserted at the 5' end of the EGFP in a pcDNA3.1(-) vector containing EGFP between EcoRI and BamHI restriction sites.
The primers used for LifeAct generation are shown in the Table 2.1 below in 5' to 3' direction:

Table 2.1: Primers used for the PCR of LifeAct-EGFP construct.

XbaI-LifeAct-Forward	GTTGTTGTTTCTAGAATGGGCGTGGCCGACTTG ATCAAGAAGTTCGAGTCCATCTCCAAG
EcoRI-LifeAct-Reverse	GTTGTTGTTGAATTCGGTGGCGACCGGTGGAT CCCCCTCCTCCTTGGAGATGGACTCGAA

2.2.2 PCR reaction conditions

The PCR reaction components and conditions for the generation of the LifeAct sequence with its linker are given below. A two-step PCR was used since in the beginning the annealing regions are short and then, as the reaction progresses, the annealing regions become longer. After the PCR reaction, the product was loaded in agarose gel for size control and isolation. The gel was prepared using 2% agarose (w/v) with TAE buffer and 0.5 μg/mL Ethidium Bromide for visualization. An appropriate DNA Ladder was loaded in one lane. The gel was run at 100V for 45 minutes in 1X TAE

buffer. The desired band was then excised from the gel under UV illumination and isolated using Qiagen Gel Extraction Kit (Cat no. 28704) according to the manufacturer's instructions.

Table 2.2: PCR mixture for the construction of LifeAct

Component	Volume
Phire green Master Mix	25 μL
Forward primer XbaI-LifeAct-Forward	1.5 μL
Reverse primer EcoRI-LifeAct-Reverse	1.5 μL
Nuclease free water	22 μL

Table 2.3: PCR conditions for the construction of LifeAct

Initial denaturation	98°C	30 sec	
Denaturation	98°C	10 sec	6 X
Annealing	45°C	30 sec	
Extension	98°C	10 sec	
Denaturation	98°C	10 sec	30 X
Annealing	70°C	30 sec	
Extension	98°C	10 sec	
Final extension	98°C	5 min	

2.2.3 Restriction digestion

Restriction digestion of the PCR products and vectors was carried out in order to generate sticky ends for the subsequent ligation reaction. Restriction enzymes were purchased from New England Biolabs (NEB). The protocol outlined in Table 2.4 was followed. The digestion reaction was carried out for 2 hours at 37°C. After the digestion procedure, the products were loaded in 2% agarose gel and run at 100V for 30 minutes in order to obtain clear bands. The bands were excised under UV and isolated using Qiagen Gel extraction kit according to the manufacturer's instructions.

Table 2.4: Digestion protocol for LifeAct PCR product and EGFP in pcDNA3.1(-) vector

Component	Volume
Water	9.1 μL
10X Buffer	1.5 μL
LifeAct DNA	4 μL
XbaI	0.2 μL
EcoRI	0.2 μL

Component	Volume
Water	9.1 μL
10X Buffer	1.5 μL
EGFP in pcDNA3.1(-)	4 μL
Xbal	0.2 μL
EcoRI	0.2 μL

2.2.4 Ligation

The plasmid and insert DNA were measured using Nanodrop (Biodrop μLITE). After the determination of the amount and purity of the DNA, a ligation reaction was set up in order to ligate the sticky ends of the insert and the vector. T4 DNA Ligase from NEB (Cat no. 0202T) was used according to the manufacturer's instructions. 1:10 and 1:20 vector:insert ratios were used. 100 ng vector was used for all ligations. All reactions were incubated for 5 hours at room temperature. The reaction protocol is given in Table 2.5.

Table 2.5: Ligation protocol for LifeAct ligation to EGFP in pcDNA3.1(-)

	1: 10	1: 20	Control
LifeAct	4 μL	8 μL	-
EGFP in pcDNA	1 μL	1 μL	1 μL
Buffer	2 μL	2 μL	2 μL
T4	1 μL	1 μL	1 μL
Nuclease free water	12 μL	8 μL	16 μL

2.2.5 Isolation of positive ligation products using competent E. *coli* cells

Competent E. coli cells were transformed with the ligation products following the ligation reaction. A heat shock method was used under aseptic conditions on the bench. Shortly, competent E. coli DH5 cells were taken from the -80°C freezer and thawed on ice for 10 minutes. 3 μL ligation product was added to the cells, and they were incubated on ice for 30 minutes. Afterwards, cells were placed in 42°C heat block for 45 seconds, and then incubated on ice for 5 more minutes. After this incubation, Lysogeny broth (LB) was added to complete the volume to 1 mL and the cells were grown in 37°C with constant shaking for 1 hour. Afterwards, the cells were centrifuged at 6000 rpm for 3 minutes and 800 µL of the supernatant was removed. The cell pellet was resuspended in the remaining 200 μL LB and inoculated onto selective agar media (with Ampicillin) using glass beads. The agar plates were incubated overnight (16 hours) at 37°C. The next day, single colonies from the agar plates were each inoculated to 4 mL selective liquid media (LB with Ampicillin) in blood tubes. The liquid cultures were grown overnight (16 hours) at 37°C with constant agitation. The next day, the plasmids from each tube were isolated using Thermo Scienfitic GeneJET Plasmid Miniprep Kit (Cat no. K0503) following the manufacturer's instructions. The purity and quantity of the plasmid DNA was checked using Nanodrop. The isolated plasmids were sent for sequencing to verify the correct LifeAct sequence. The constructs with the correct sequence were used for cell culture studies.

2.3 Cell culture

2.3.1 Cell maintenance and passage

Neuro-2A neuroblastoma cell line purchased from ATCC (ATCC® CCL-131TM) was used for all experiments. The cells were maintained in complete medium containing 44,5% Dulbecco's Modified Eagle Medium (DMEM, Gibco Cat no. 11965092), 44,5% reduced serum medium (OptiMEM, Gibco Cat no. 31985070), 10% Fetal Bovine Serum (FBS, Gibco Cat no. 10500056) and 1% Antibiotic (Penicillin/Streptomycin) and grown in standard 25 cm^2 cell culture flasks in a 37°C and 5% CO_2

incubator (Nuve EC 160). All cell procedures were carried out at a laminar flow hood. The cells were split twice weekly, using Phosphate-Buffered Saline (PBS) for wash and TrypLE^{TM} Express (Gibco, Cat no. 12605028) as dissociation reagent. Shortly, the flask containing confluent cells was taken to the laminar flow hood. The cell medium was aspirated, and the cells were washed with 3 mL PBS. Then, the cells were lifted from the bottom of the flask using 0.5 mL TrypLE, incubated at 37°C for 5 minutes. Meanwhile, 8 mL fresh medium was added to a new flask. When the TrypLE incubation time was complete, 8 mL fresh medium was added to the flask, the cells were mixed gently but thoroughly to break any remaining clumps, and 200 μL cells were transferred to the new flask. For each experiment, 75.000 cells cells were seeded onto a plastic cell culture dish to transfect the next day using EGFP or mCherry-tagged constructs. For cell seeding, 10 μL cells from the old flask were counted using a hemocytometer. The cells in all four 4x4 squares were counted and averaged. The cell number was calculated as follows:

$$\text{Number of cells } /mL = \frac{\text{Number of total counted cells}}{4} \times 10^4$$

2.3.2 Transfection of cells with fluorescent constructs

Transient transfection was carried out using Lipofectamine LTX^{TM} (Invitrogen, Cat no. 15338100) according to the manufacturer's protocol. Shortly, 500 ng of each DNA was diluted in 100 μL OptiMEM in a 0.5mL tube; 4 μL PlusTM reagent was added and the solution was incubated for 15 minutes. Next, 4 μL Lipofectamine LTX^{TM} was diluted in 100 μL OptiMEM separately and then added to the OptiMEM-DNA-Plus reagent tube and incubated for 15 more minutes. Meanwhile, cells were washed once with PBS and 800 μL OptiMEM was added to the dish. Afterwards, the DNA containing mixture was added to the cells. The dish was taken to the CO_2 incubator for 3 hours to allow for plasmid entry. After 3 hours, 2 mL media was added, and the cells were left to grow for 24 more hours.

2.3.3 Cell seeding to silicon substrates

Before cell seeding, previously cleaned silicon substrates were placed into 35 mm plastic bottom cell culture dishes and sterilized with 70% EtOH and 15-minute UV exposure. Afterwards, the substrates were immersed in complete cell media for at least 15 minutes. The media was aspirated immediately before cell seeding. For seeding to the substrates, the cells were grown for 24 hours, then washed once with PBS and lifted using 160 μL TrypLE for 5 minutes at 37°C. Then, the cells were centrifuged at 800 rpm for 5 minutes to remove TrypLE, then resuspended again in 1 mL complete medium and counted using a hemocytometer. Afterwards, the cells were diluted in order to obtain the desired number of cells. 2 mL cell suspension was added to the 35 mm dish, assuming that the cells fall uniformly on the silicon substrates and the remaining plastic surfaces. The dishes were incubated at 37°C, 5% CO_2 until imaging.

A schematic representation of the transfection and cell seeding protocols are shown in the Figure 2.3 below.

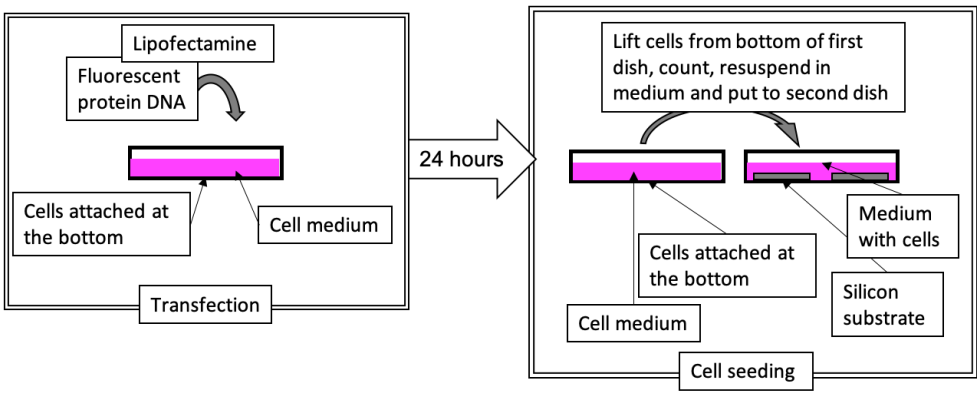

Figure 2.3: Schematic representation of the transfection and seeding protocols.

2.4 Imaging and analysis

2.4.1 Cell proliferation assessment

For the assessment of cell proliferation, 30000 cells were seeded on the wells of 24-well plates, which contained silicon substrates of 1 cm^2 area or no substrate (control plastic surface). Cells were lifted after 24, 48 and 72 hours and counted using a hemocytometer. For all wells with substrates, the substrates were taken to a clean well before trypsinization, in order to avoid counting cells in the remaining plastic areas. To correct for area differences, all cell numbers on the plastic well (surface area is 2 cm^2) were divided by 2.

2.4.2 Live imaging with fluorescence microscopy

For all fluorescence microscopy experiments, an inverted fluorescence microscope (Leica DMI4000B) equipped with a confocal setup (Andor AMH200 Metal Halide lamp, Zyla 5.5 sCMOS and DSD2 Differential spinning disc) was used. An overview of the instruments is shown in Figure 2.4

For live imaging experiments, the cells growing in 16 mm square substrates were taken after 3- or 24-hours incubation, washed once with Hank's Buffer with HEPES (HHBS) and transferred upside down onto a glass bottom cell culture dish. The 16 mm size was chosen because the glass part of glass bottom dish was measured to be roughly 2 cm. In this way, the 4 corners of the silicon substrates could stand on the plastic part. The glass bottom dish is shown in the Figure 2.5 below. The dishes have a coverslip region which is lower than the plastic region. This way, the cells could remain suspended in upside down fashion, while still having access to media and nutrient flow. The protocol is shown in more detail in the Figures below. Figure 2.6 shows a schematic representation of how the 16 mm square substrates were positioned on the glass bottom dish. The cell medium is not shown for simplicity, however complete media was present when the cells were imaged with time-lapse microscopy. Since the objective of the microscope is located at the bottom side (inverted microscope), the substrates were positioned upside down such that the cells

Figure 2.4: Image of the microscope components showing A: Andor AMH200 Metal Halide lamp, B: Zyla 5.5 sCMOS and DSD2 Differential spinning disc and C: Leica DMI4000B.

were at the bottom side, between the coverslip and the substrate.

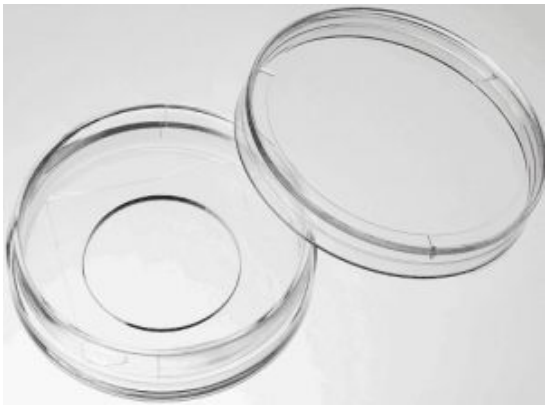

Figure 2.5: Commercial glass bottom cell culture dish used in this study.

The dish was taken to the live-imaging apparatus on the microscope and time-lapse experiments were carried out with cells maintained in 37°C and 5% CO_2 throughout the experiments. The setup was equipped with appropriate filters for EGFP. Time-lapse videos were taken using 10X objective and each region was imaged for 60 minutes. Figure 2.7 shows the experimental setup for the live imaging. The 37°C and 5% CO_2 conditions were sustained through the appropriate instruments, which were

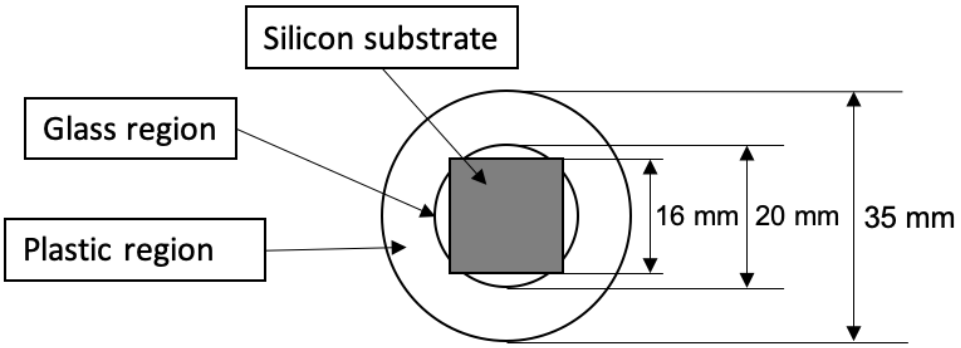

Figure 2.6: Schematic representation showing the positioning of the silicon substrates on the glass bottom dish for time-lapse imaging.

connected to the live imaging apparatus. The position of the 10X objective is also shown in the scheme.

2.4.3 Cell fixation and fluorescence microscopy imaging

For fluorescence images, cells were first fixed using 4% formaldehyde (FA). Shortly, the media was aspirated, the cells were washed once with PBS and then 1 mL fresh media and 1 mL 4% FA was added to the cells. After 3 minutes incubation, this solution was aspirated and 2 mL 4% FA was added dropwise to the cells and incubated in the dark at room temperature for 15 minutes. Afterwards, the PFA was aspirated and the cells were washed twice with PBS to remove any remaining fixative agent. The substrates were then imaged upside down over a coverslip (No.0) using 10X or 63X oil objectives.

2.4.4 Cell dehydration and SEM imaging

For SEM imaging, cells were fixed as described above and dehydrated using increasing concentrations of ethanol (40%, 60%, 80% and 96%) for 10 minutes each. Then, the cells were dried on the bench for 24 hours and stored in a closed container until SEM imaging. Before SEM, samples were coated with 3 nm gold and lead mixture to increase surface conductivity.

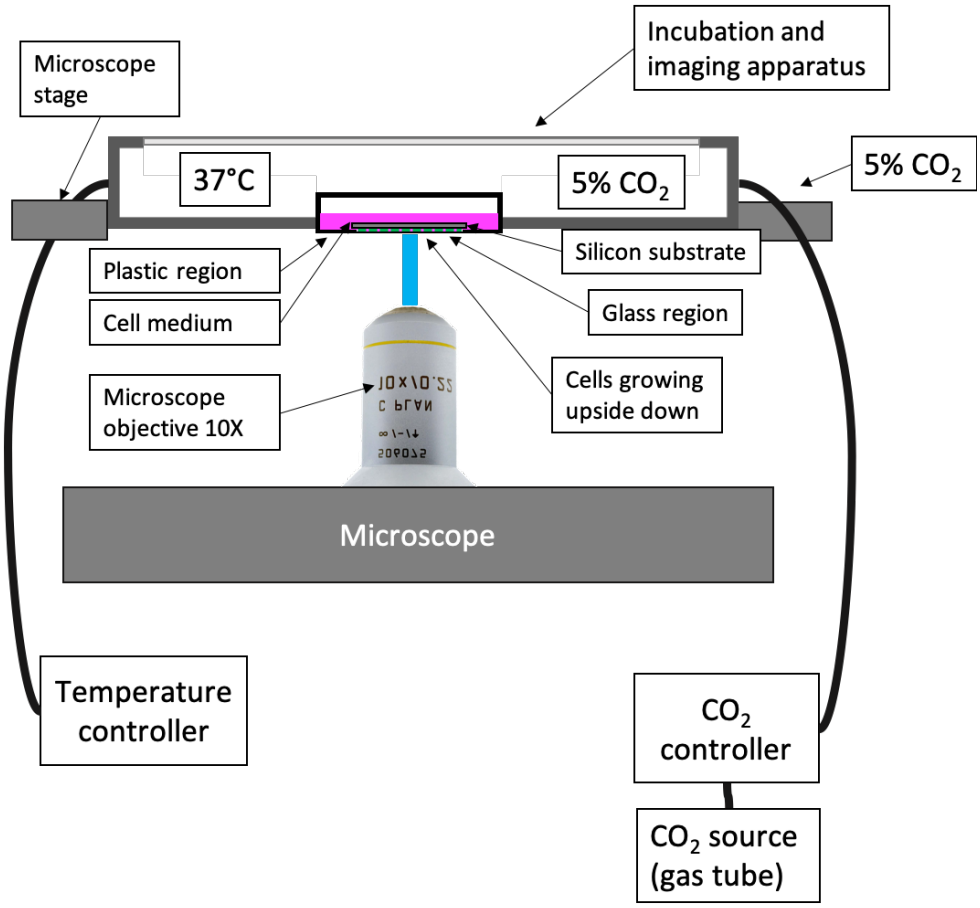

Figure 2.7: Scheme showing the live imaging setup used for the time-lapse experiments. In all experiments, 37°C and 5% CO_2 conditions were sustained throughout the duration of the experiments. The cells were upside-down in all experiments. Only the bottom part of the microscope is shown for simplicity.

2.4.5 Image and data analysis

All cell images were analyzed using ImageJ or FIJI software. Before analysis, the image scale was corrected using the "Set scale" function and taking the width of the 10X images as 1400 μm. For cell motility analysis, at least 7 cells from each region were manually tracked using the Manual Tracking Plugin. For cell alignment analysis, cells were manually counted using Cell Counter, with cells located onto line topographies and those between the lines counted as different types. For visualization of cell motility mechanisms, single cells were cropped from the time-lapse videos, and the images were compiled using ImageJ's Montage function. For cell shape analysis, sin-

gle cells from 10X or 63X images were traced manually using ImageJ's polygon tool. Then, cell area, perimeter, circularity and ellipse fit were calculated in ImageJ by using the "Measure" tool. The desired features were selected using the "Set measurements" option. For cell number analysis, ImageJ's particle analyzer plugin was used. Shortly, nucleus images were converted to 8-bit and thresholded manually. Then, the particle analyzer tool was run using a minimal size of 50 pixels. Images with large cell clumps were not used. All statistical analyses were performed in Graphpad Prism 8 using Mann-Whitney non-parametric tests for each pair.

CHAPTER 3

RESULTS AND DISCUSSION

3.1 Substrate structuring and characterization

Control on laser fluence was exerted by changing the scanning velocity of the beam, which in turn controlled the number of shots (N) falling onto each spot. Small shot number (N<10) resulted in LIPSS, grating-like structures with wavelengths comparable to the irradiation wavelength (referred to as low spatial frequency LIPSS, or LSFL) [45, 4]. LIPSS formation is known to involve feedback loops. In the case of ablation-type LIPSS, a positive feedback loop aids in the formation of the periodic structures, however, no negative feedback loop is present to stabilize the effects and the periodicity may be lost as further laser shots are delivered to the area. This way microcolumn-like structures can grow. The process is shown in Figure 3.1.

A similar effect was achieved in the present study, with 2 or more passes resulting in extensive periodicity loss and the formation of microcolumns. Figure 3.2 shows the SEM images of the surface irradiated with 1,2 and 3 pulses. For the current setup, a

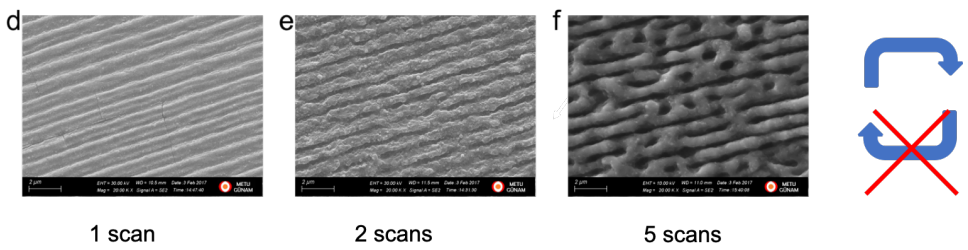

Figure 3.1: SEM images showing the change in substrate topography and the gradual formation of microcolumns from LIPSS topography. Adapted from Pavlov et al. [45]

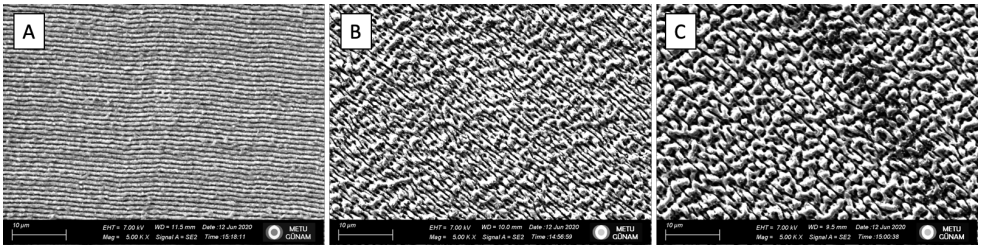

Figure 3.2: SEM images showing the change in substrate topography and the gradual formation of microcolumns from LIPSS topography.

power of 360 mW on the substrate and a velocity of 1500 mm/s resulted in LIPSS, as seen in Figure 3.2 part A. A second scan of the same area resulted in the growth of some microcolumns, while some periodic structures remained, as seen in part B. A third pass caused further column growth and the loss of periodicity, as seen in part C. Similar to Figure 3.1 and to the theory, an increased number of shots resulted in microcolumn formation.

Microcolumn topography was also achieved directly by controlling the number of shots delivered to an area through the scan velocity. Whereas fast scans (1500 mm/s and above) resulted in LIPSS, slower scans resulted in microcolumns. 100 mm/s was used for microcolumns in this study. SEM images of LIPSS generated in our study can be seen in Figures 3.3 part A and in Figure 3.4

LIPSS are highly regular structures resembling a grating structure formed by lithography, but with smooth edges. The regularity and homogeneity of LIPSS can be seen in Figure 3.3 part A and in Figure 3.4. The groove depths are around 300 nm, and the whole structure is covered in nano-scale roughness. The direction of LIPSS could be controlled by controlling the beam polarization. The LIPSS generated was ablation type with direction normal to the laser polarization. As predicted by theory, higher fluences resulted in micro-column or coral-like structures [78, 50]. The microcolumns generated in the present study can be seen in the SEM image in Figure 3.3 B. As shown in the SEM image, these microcolumns have small sizes (widths in the order of 1 μm), so a single cell (about 10 μm) would spread on multiple columns. A few studies of cells on microcolumns of various sizes are available in literature. In the present study, the shape of the microcolumns was affected by the fluence. For lower

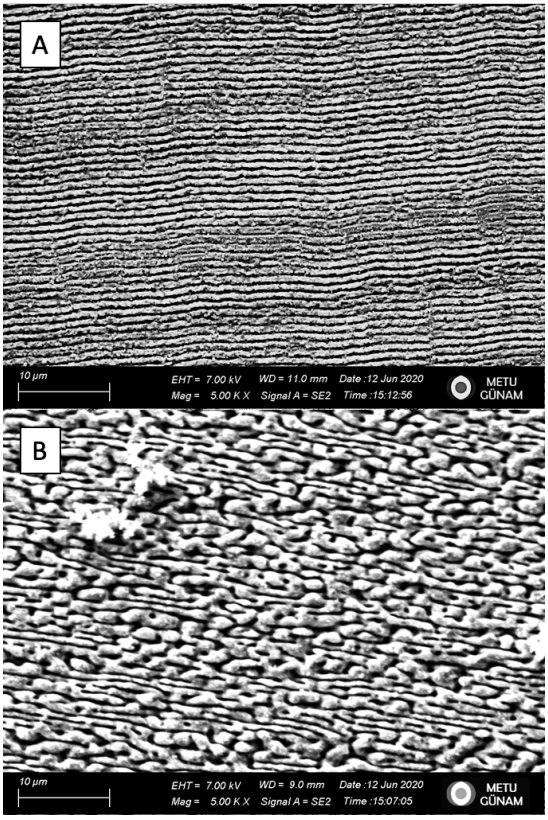

Figure 3.3: SEM image of LIPSS (A) and microcolumn topography (B) generated on silicon. Magnification: 5000X

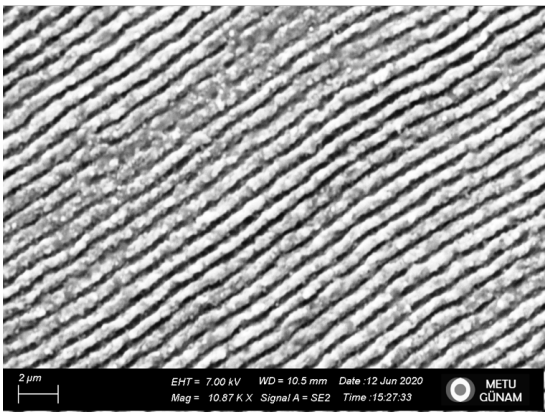

Figure 3.4: SEM image of LIPSS. Magnification: 10870X

fluences or power, the microcolumn areas included ripple-like regions. For higher powers, the ripple-like regions disappear, and only column-like features are seen.

AFM can give further details about the substrate topography, such as height information and surface roughness. The depth of the ridges in LIPSS as well as the heights of the microcolumns can be measured reliably with AFM, provided that they don't exceed 2 μm. In Figure 3.5 the results of the AFM measurements of LIPSS and microcolumn topographies are shown. The 3D views (A and B) show a render of the measured substrate in 3D. In both figures, the z axis has been scaled so that it is roughly proportional to the x and y dimensions. The 2D views (C and D) show the measured substrate area in a plot where lighter color represents higher z measurement. The line profiles (E and F) show the heights measured on a line selected from the 2D image. It can be seen that LIPSS have roughly regular ridges with heights on the range 250-400 nm. On the other hand, the microcolumns have heights as large as 800 nm.

The surface roughness can be calculated by considering all the height measurements in each pixel of the image. Different calculations lead to different types of roughness such as Ra or Rrms. In several studies concerning cells, Ra is used; therefore Ra has been reported in the present study as well. AFM software automatically calculates various types of roughness measures. On LIPSS, Ra roughness was found to be 80 nm, while on microcolumns it was found as 140 nm.

3.2 General cell behavior on polished, LIPSS and Microcolumn topographies

3.2.1 After 3 hours

3.2.1.1 Cell adhesion

SEM imaging was employed in order to observe how cells adhered to the different substrate topographies. SEM allows simultaneous visualization of the cells and the background, while offering higher resolution than confocal microscopy.

Cells growing on polished silicon, LIPSS and microcolumns for 6 hours are shown

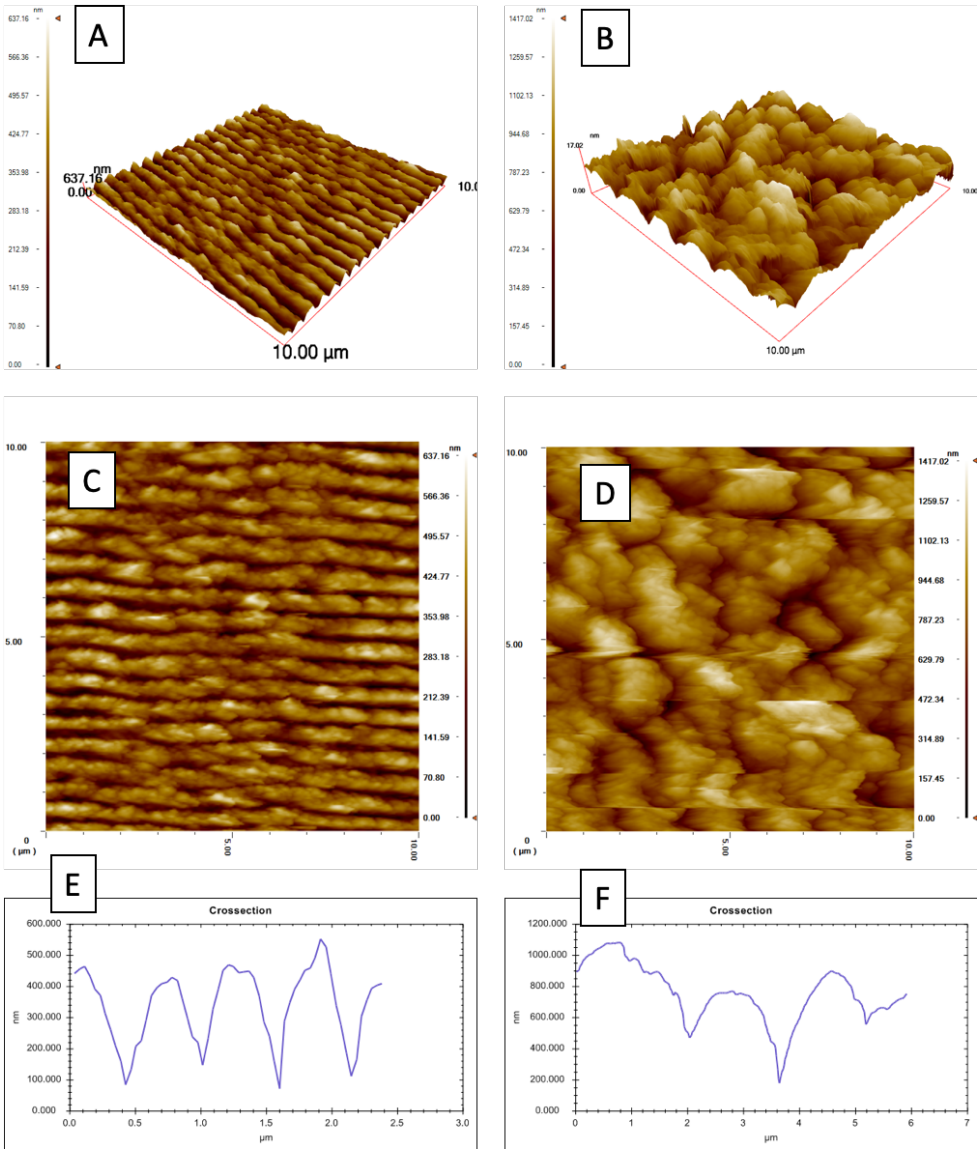

Figure 3.5: AFM measurements for LIPSS (A,C,E) and microcolumns (B,D,F). A,B show 3D topography, C,D show 2D image and E,F show the cross section of a randomly chosen line.

in Figure 3.6. SEM shows the surface of the cells and substrate, as seen from above. All images were taken with no tilt angle, directly perpendicular to the surface. In the images, darker regions represent depressions, holes and grooves. Cells which look whiter have larger height. It is clear from the images that cells interact with all topographies in a short time. However, some are more spread out (darker color) while some are less spread out and have less contact with the substrate. LIPSS did not elicit any pseudopodia alignment, as seen in part C, with cell projections extending in multiple directions.

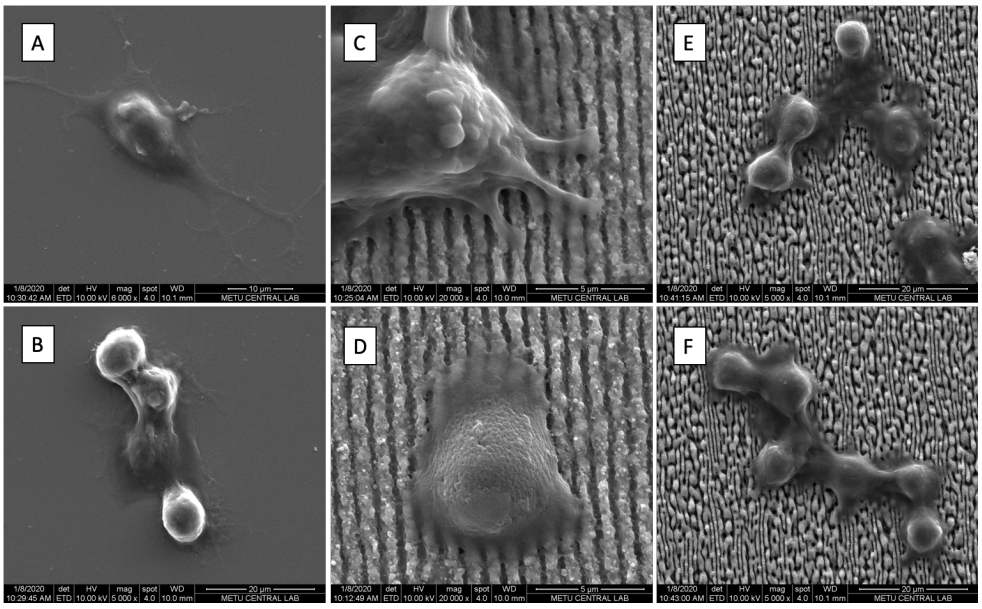

Figure 3.6: SEM image of cells on polished silicon (A,B), LIPSS (C,D) and Microcolumns (E,F)

Although cells interacted with all topographies, cell numbers on the different topographies were different. Initial adhesion was found to be significantly less on polished silicon than on all other structured substrates. Initial cell adhesion was found to be strongest on the Microcolumn topography. This observation was used in order to design an experiment for cell patterning. Cells were seeded onto a substrate with flat and structured regions and incubated for three hours. Then, the substrate was washed and taken to the imaging chamber. This allowed for cell patterning, such as shown in Figures 3.7 and 3.8

Figures 3.7 and 3.8 are from two different experiments on different substrates and

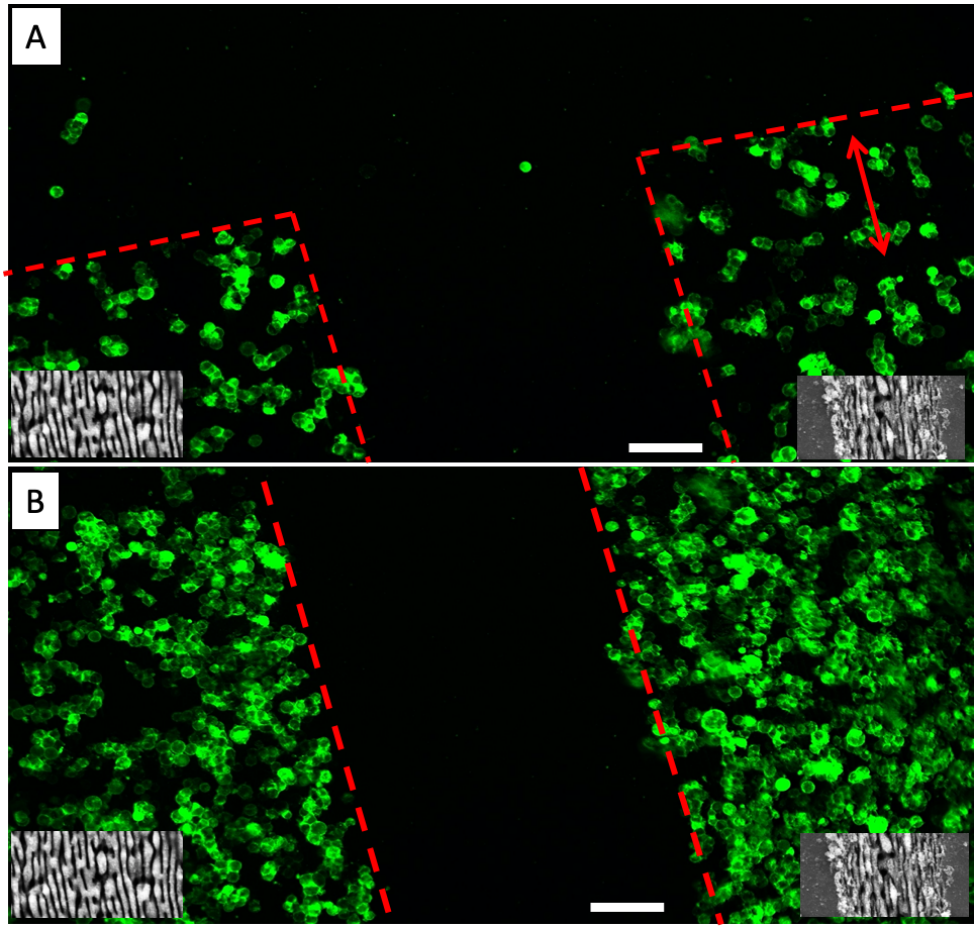

Figure 3.7: Fluorescence microscope image of cells transfected with membrane-targeted EGFP, 3 hours after seeding. Red lines show the border between structured regions and unstructured (polished) regions. Red arrow in A shows the direction of the microcolumn trench lines. Both images A and B show different ROI from the same sample. In each case, cells are found more on whole area microcolumns (left) and microcolumn trench lines on polished silicon (right) than on unstructured, polished silicon (middle). All scale bars are 100 μm.

different days.

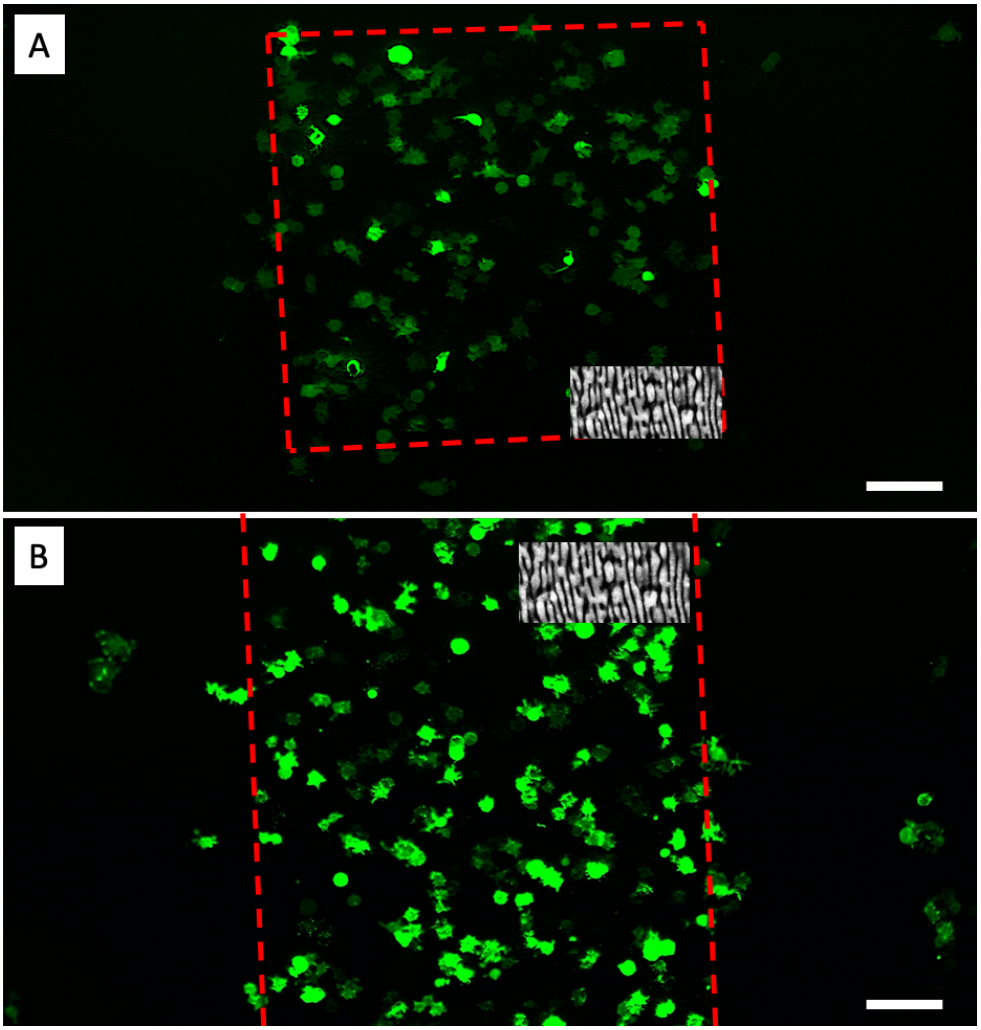

Figure 3.8: Fluorescence microscope image of cells transfected with membrane-targeted EGFP, 3 hours after seeding. Red lines show the border between structured regions and unstructured (polished) regions. Both images A and B show different ROI from the same sample. In each case, cells are found more on whole area micro-columns than on unstructured, polished silicon (other regions). All scale bars are 100 μm.

The cell patterning persists for at least 3 hours on the substrates; however, the patterning does not persist when cells are grown upside down on the substrate for 24 more hours, as cells eventually move out of the structured areas.

3.2.1.2 Cell motility and exploration behavior

Cell motility and exploration behaviors after 3 hours were also observed. Cells were recorded for 1 hour each on glass, polished silicon, LIPSS and microcolumn topographies. The time-lapse videos showed differences in cell motility and velocity. On polished silicon, some cells show lamellipodia-based motion and exploration, with a large lamellipodium protruding from one side of the cell as shown in Figure 3.9. The same motility is also visible on glass, suggesting that cell motility mechanisms on flat silicon are similar to the standard culture substrate material. Montage of a cell moting on glass is shown in Figure 3.10

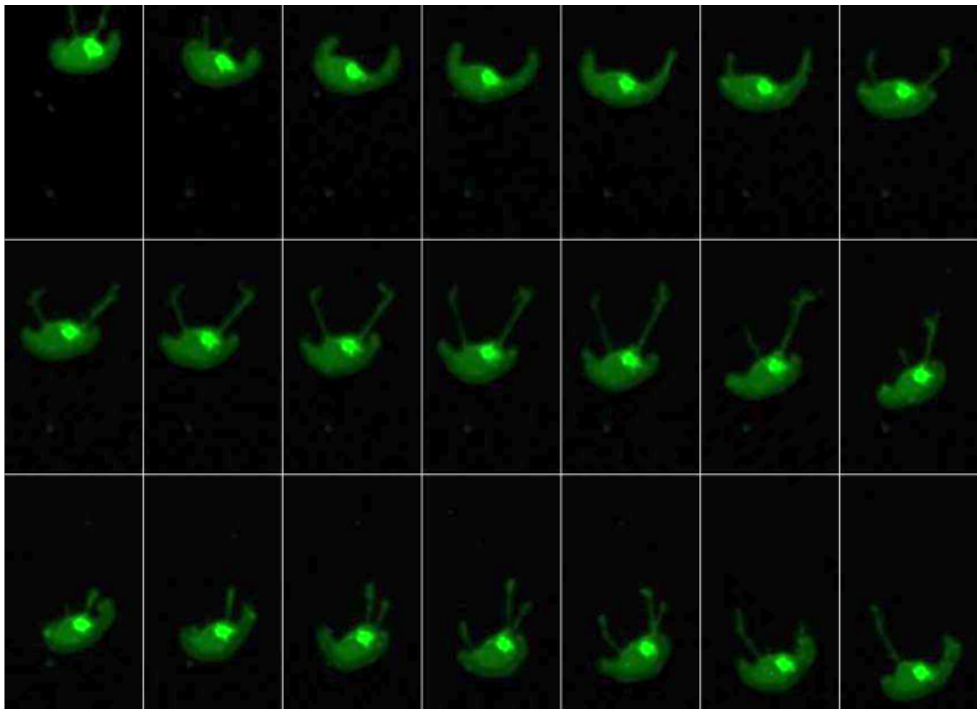

Figure 3.9: A cell on polished silicon showing lamellipodia-based motility. The images shown insets of time-lapse videos showing cells moving on polished silicon. The time-lapse had a duration of one hour. The cells had been transiently transfected with membrane localized EGFP. The time-lapse videos were taken using 10X objective in an inverted microscope.

On flat silicon, uniform anisotropic lamellipodia were also observed on some cells. On the other hand, on structured surfaces, this type of shape was not observed; cells remained mostly circular or elliptical and extended lamellipodia or filopodia in all

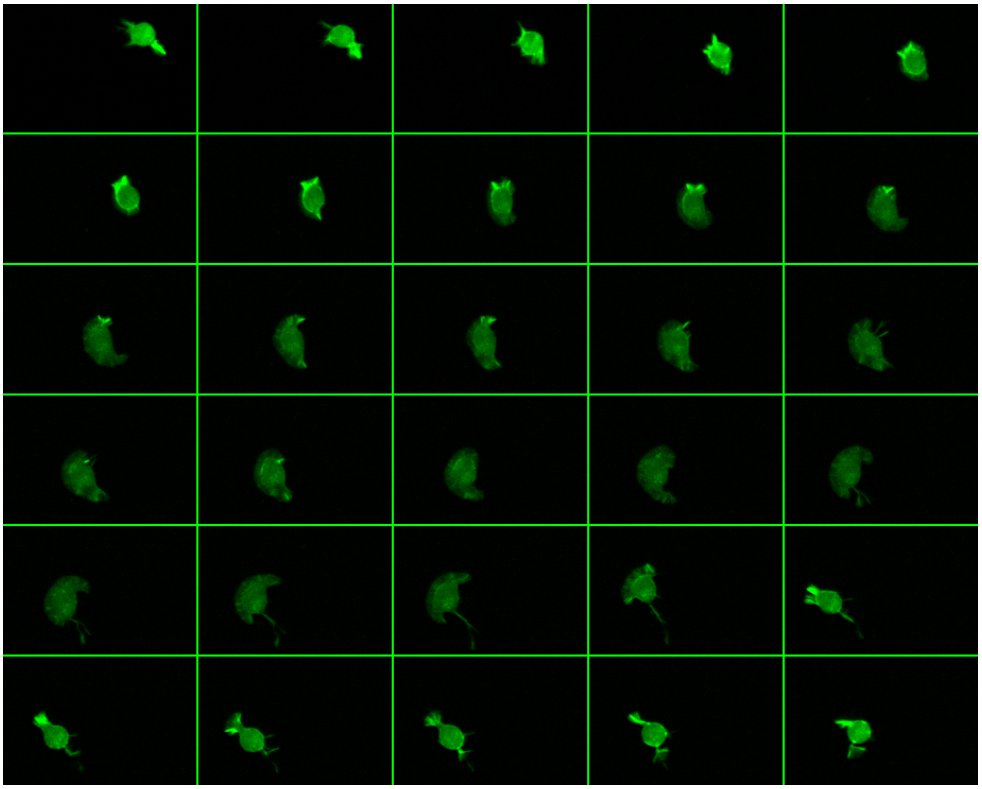

Figure 3.10: A cell on glass showing lamellipodia-based motility. The images shown insets of time-lapse videos showing cells moving on glass. The time-lapse had a duration of one hour. The cells had been transiently transfected with membrane localized EGFP. The time-lapse videos were taken using 10X objective in an inverted microscope.

directions. Circular shape signifies low spreading and less contact with the substrate. Elliptical shape is the usual and expected shape for this cell type, Neuro-2A cells have elliptical/teardrop-like shape when cultured on glass substrates.

Time-lapse experiments also showed that cells moved with different velocities on the three considered topographies. To analyze cell motility, single cells from the time-lapse videos were tracked manually using ImageJ. The tool allows the user to click on one cell in every frame, and it stores the coordinates of the cell for each frame. The velocity and position in each frame are analyzed automatically. The tool reports the coordinates (in pixels), distances and velocities in a list. The fastest motility was seen on polished silicon, with cells moving, on average, at least twice as fast as those on structured regions. The slowest motion was seen on the microcolumns, with very

minimal motility. The results for cell velocity are summarized in Table 3.1 and Figure 3.11.

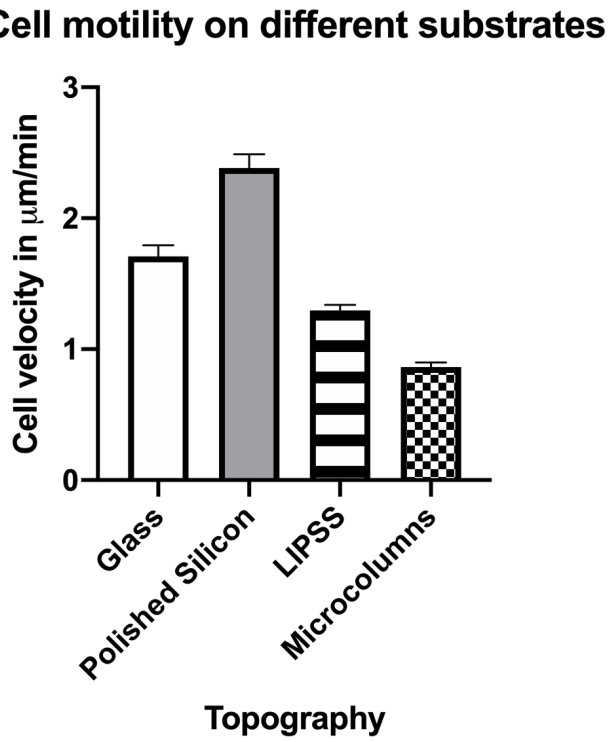

Figure 3.11: Bar graph of average cell velocities in microns/minute on glass, polished silicon, LIPSS and whole area microcolumn topographies. Values are shown as Mean + SEM.

It is possible that the microcolumn topography offers many nanoscale features that cells could interact with, and that this adhesion together with roughness hinders cell movement. Conversely, polished silicon may offer less roughness features for adhesion and less obstacles to motility, resulting in lower resistance to wash assay and higher cell velocity. In general, cell motility is maximized for certain adhesion ranges. It was outlined in the introduction chapter that cell motility involves the formation of new adhesion points at the leading edge and the detachment of adhesions at the rear end of the cell. If adhesion to the substrate is too high, then the rear adhesion detachment is lowered and so is cell motility. On the other hand, if cell adhesion to the substrate is too low, the cells can also not move onto the substrate due to inability to form new adhesions.

Table 3.1: Average velocities of cells on different substrates. The data is shown as Mean ± SEM

Glass	1.71 ± 0.08 μm/min
Polished silicon	2.38 ± 0.10 μm/min
LIPSS	1.29 ± 0.04 μm/min
Microcolumn	0.86 ± 0.03 μm/min

Due to the directionality of LIPSS, there was the possibility of having directional migration of cells on the LIPSS structure. To test that, the trajectories of several cells were extracted from the coordinate data and plotted in an xy-graph. In addition, cell directionality was calculated by dividing the total displacement of each cell by the total distance traveled. The results of the trajectories are shown in Figure 3.12 below, with cells on flat substrates shown in the left (blue) and cells on LIPSS shown in the right (green). The LIPSS direction was vertically. Interestingly, the cells did not show directed migration in the LIPSS direction. The directionality was found to be around 0.33 ± 0.18 for cells on both flat and LIPSS topographies, suggesting no directional migration on the LIPSS for the time frame considered. Directional migration was previously reported for C6 glioma cells on LIPSS structures [79]. However, the LIPSS structure the authors used had higher aspect ratio, so this may have affected this result.

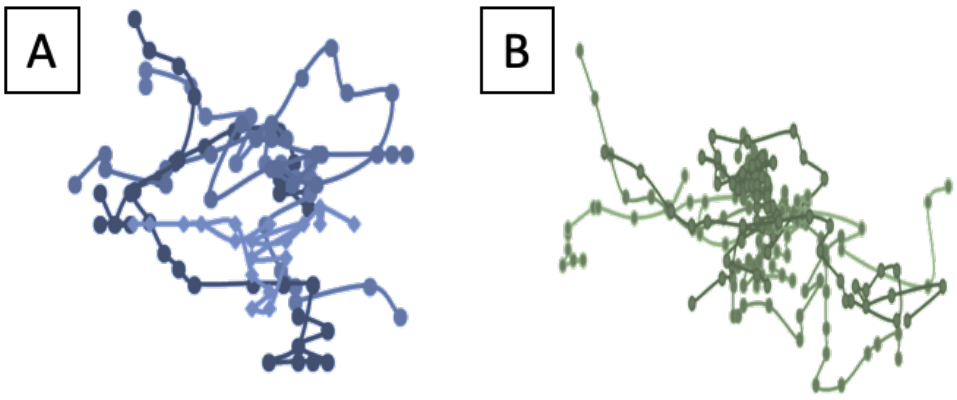

Figure 3.12: Trajectories of cells on polished silicon (A) and vertically oriented LIPSS (B).

3.2.2 Cell response after 24 hours

Cell adhesion on the substrates after 24 hours was analyzed on fixed cells using fluorescence microscopy. Cell number, cell shape, actin cytoskeleton and stress fiber formation were analyzed.

3.2.2.1 Cell proliferation

Cell proliferation was evaluated after 24 hours, 48 hours and 72 hours on plastic, polished silicon, LIPSS and microcolumn topographies, by counting the cells on each substrate. The results are summarized in the Figures 3.13 and 3.14 in linear and log scales, respectively.

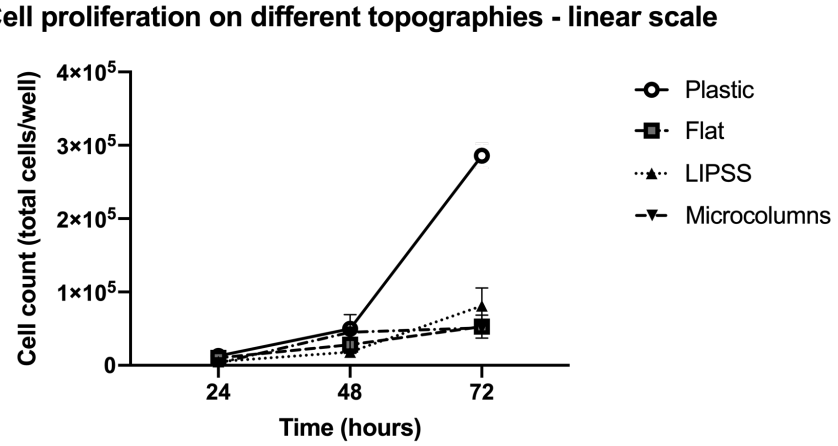

Figure 3.13: Cell numbers after 24, 48 and 72 hours on plastic, polished silicon, LIPSS and microcolumn topographies. The cells were counted using a hemocytometer. At least three replicates are shown for each experiment.

Cell proliferation was found to be much lower on all silicon substrates, as shown by the linear plot. However, cells seem to divide on silicon substrates, too, as can be seen in the logarithmic plot. Cell proliferation was previously shown to be decreased on polished silicon, however the authors had reported the cell number on silicon to be almost constant [70]. On the other hand, our data shows some proliferation on all silicon substrates. The laser structuring did not seem to affect the proliferation either positively or negatively, compared to polished silicon.

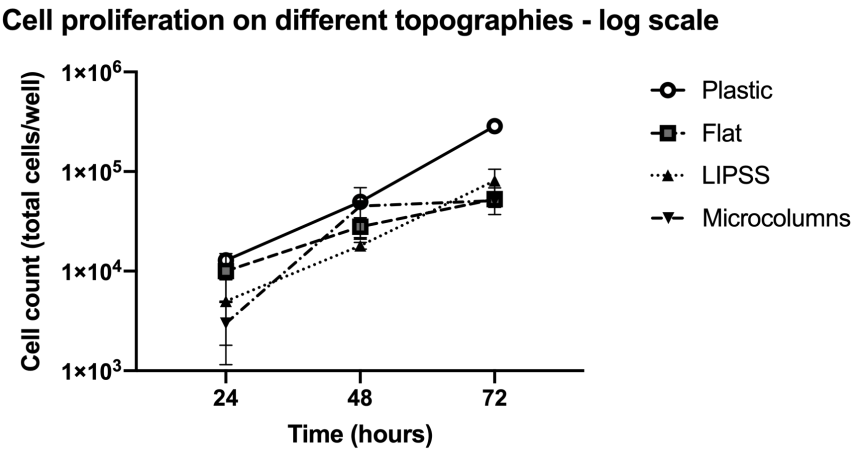

Figure 3.14: Cell numbers after 24, 48 and 72 hours on plastic, polished silicon, LIPSS and microcolumn topographies. The cells were counted using a hemocytometer. At least three replicates are shown for each experiment.

3.2.2.2 Cell number

Cells were grown on substrates with flat, LIPSS and microcolumn regions for 24 hours. Interestingly, cell preferences for the polished and structured regions changed from the initial preferences. The cells were counted automatically from separate frames on flat or LIPSS regions. The cell counting was performed automatically on manually thresholded images of NLS-mCherry (nuclei) using ImageJ's Analyze Particles tool. No differences in cell number were observed after 24 hour incubation. However, cell numbers on all silicon substrates were lower than those on plastic or glass (data not shown). Representative images of cells growing for 24 hours on polished silicon, LIPSS and microcolumns are shown in Figure 3.15

In the present study, no significant difference in cell numbers was found among the three topographies. The cell numbers were calculated from 6 different ROIs on 2 different samples. The data is summarized in Figure 3.16 and Table 3.2.

There is conflicting evidence in the literature regarding cell reactions to LIPSS topography, as outlined in the literature. Some studies have found cell migration out of LIPSS structures [80, 68] while others have found that cells are able to adhere to LIPSS [79, 67, 81, 66]. Of course, these contradictions could be due to differences in

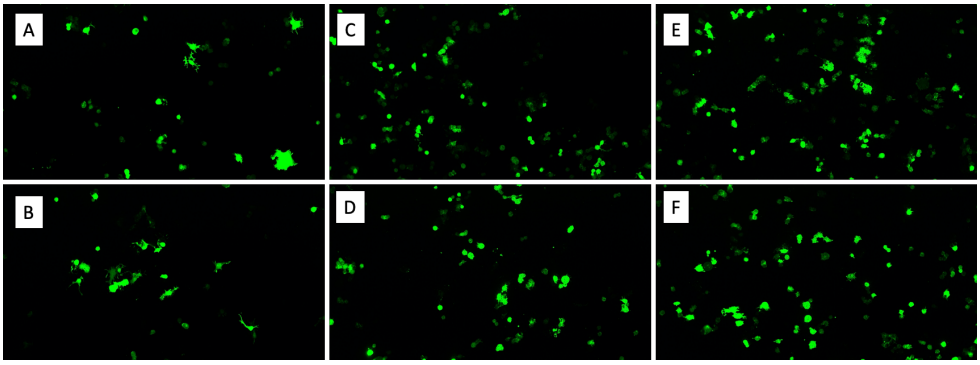

Figure 3.15: Fluorescence images of cells growing for polished silicon (A,B), LIPSS (C,D) and microcolumns (E,F). Cells were expressing LifeAct-EGFP and had been growing in complete medium for 24 hours. The images were taken using a 10X objective.

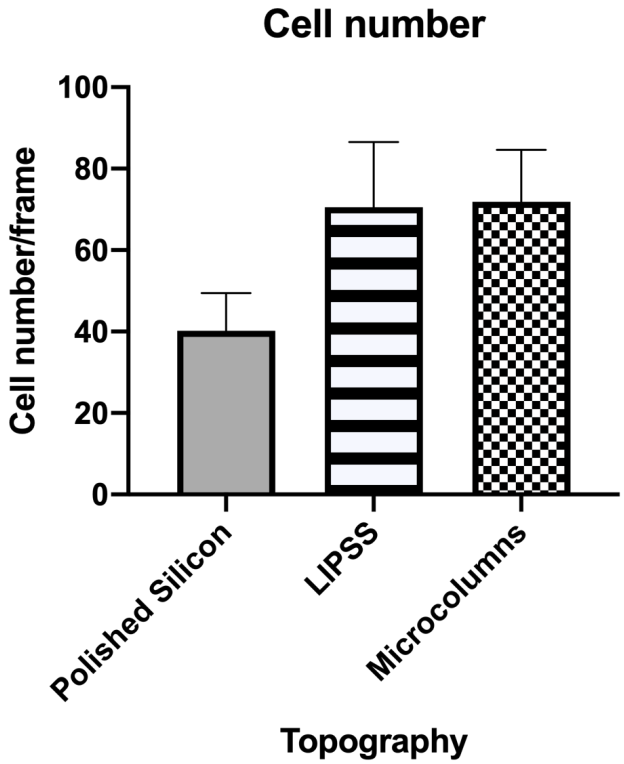

Figure 3.16: :Bar graph of average cell number on polished silicon, LIPSS and microcolumn topographies. Values are shown as Mean + SEM.

cell types, material, and LIPSS parameters (periodicity, groove depth). Aligned nanotopography was previously found to promote migration in glioblastoma cells [82].

Table 3.2: Average cell number on Polished silicon, LIPSS and microcolumn topographies. The data is shown as Mean ± SEM

Polished silicon	40 ± 9 cells
LIPSS	70 ± 16 cells
Microcolumn	71 ± 13 cells

3.2.2.3 Cell shape

The cell area, perimeter and circularity were analyzed using ImageJ from cell images on glass, polished silicon, LIPSS and microcolumn topographies. The cells were selected manually from images of cells transfected with Lifeact-EGFP and analyzed with ImageJ. Cell area analysis is summarized in Figure 3.17 and Table 3.3. Cell perimeter analysis is summarized in Figure 3.18 and Table 3.5. Cell circularity analysis is summarized in Figure 3.19 and Table 3.7. All statistical tests were carried out using Mann-Whitney non-parametric tests, as not all data was normally distributed. The results are shown in Tables 3.4, 3.6 and 3.8.

Table 3.3: Average area of cells on different substrates. The data is shown as Mean ± SEM

Glass	461 ± 31 μm^2
Polished silicon	687 ± 61 μm^2
LIPSS	587 ± 35 μm^2
Microcolumn	501 ± 21 μm^2

Cell circularity is a cell shape descriptor related to the ratio of area to perimeter, with a circle having a circularity of 1. For cells, higher circularity values for cells denote a more rounded shape and less protrusion, and is related to low adhesion and migration [83]. Lower circularity values would indicate better cell spreading and stronger interaction with the environment, higher number of neurites, or higher number of filopodia. In the present study, no difference was found in the circularity, suggesting no significant difference between the substrates in this regard. However, cells on polished silicon and LIPSS were found to have significantly larger areas and

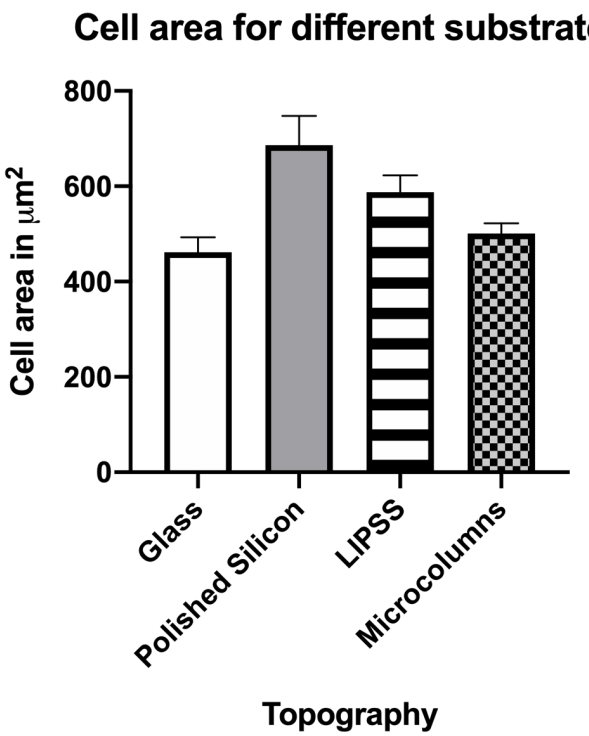

Figure 3.17: :Bar graph of average cell area on glass, polished silicon, LIPSS and microcolumn topographies. Values are shown as Mean + SEM.

perimeters compared to those on glass and those on microcolumns. This could signal more isotropic cell spreading, as the area and perimeter both have increased.

Table 3.4: Statistical significance of the differences between the groups using Mann-Whitney test, for area. *** denotes $p < 0.001$, ** denotes $p < 0.01$, * denotes $p < 0.05$ and ns denotes all $p > 0.05$.

	Polished	LIPSS	Microcolumns
Glass	***	***	ns
Polished		ns	ns
LIPSS			ns

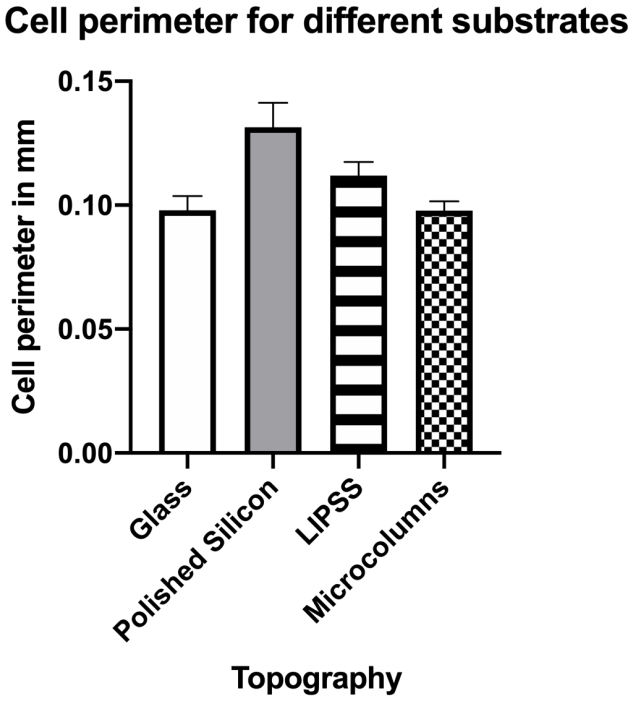

Figure 3.18: :Bar graph of average cell perimeter on glass, polished silicon, LIPSS and microcolumn topographies. Values are shown as Mean + SEM.

3.2.2.4 Actin cytoskeleton

To observe the actin cytoskeleton, cells transfected with LifeAct-EGFP were grown on silicon substrates for 24 hours, fixed and imaged using confocal microscopy. Confocal images showed good cell spreading and stress fiber formation in cells on polished silicon, both in complete and 1% FBS medium. Images of LifeAct-transfected cells on flat silicon and differentiation medium are shown in Figure X. Stress fiber

Table 3.5: Average perimeter of cells on different substrates. The data is shown as Mean ± SEM

Glass	0.100 ± 0.005 mm
Polished silicon	0.132 ± 0.010 mm
LIPSS	0.120 ± 0.005 mm
Microcolumn	0.098 ± 0.004 mm

Table 3.6: Statistical significance of the differences between the groups using Mann-Whitney test, for perimeter. *** denotes $p < 0.001$, ** denotes $p < 0.01$, * denotes $p < 0.05$ and ns denotes all $p > 0.05$.

	Polished	LIPSS	Microcolumns
Glass	***	**	ns
Polished		ns	ns
LIPSS			ns

formation in the edges of the cells can be seen in Figure 3.20. Some cells show stress fiber formation in the cell body as well. Some cells also show neurite formation. These suggest that cells are able to adhere to silicon after 24 hours, even when cultured in low serum conditions.

Figure 3.21 below shows confocal images of cells grown on polished, LIPSS and microcolumn topographies, for 24 hours in complete medium. Differences in cell size, shape and stress fibers are visible. Flat regions seem to allow thicker stress fiber for-

Table 3.7: Average circularity of cells on different substrates. The data is shown as Mean ± SEM

Glass	0.72 ± 0.02
Polished silicon	0.62 ± 0.03
LIPSS	0.67 ± 0.02
Microcolumn	0.62 ± 0.02

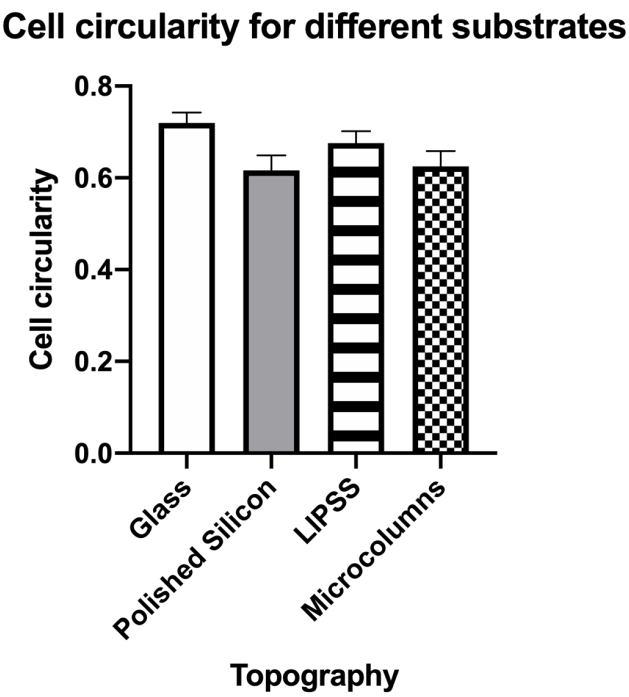

Figure 3.19: :Bar graph of average cell circularity on glass, polished silicon, LIPSS and microcolumn topographies. Values are shown as Mean + SEM.

mation, as well as adequate spreading, with cells looking less circular. Stress fiber thickness may be related to cell motility. Stress fibers are thick and stable in non-motile cells, or in cells grown in rigid substrates. In motile cells or cells grown on soft substrates, stress fibers are shorter and thinner. It is suggested that stress fiber formation limits cell motility, as the reorganization of actin from the thick stress fibers is slow [84]. On LIPSS, cells do not have prominent stress fibers. The spreading seems less, however the cells show pseudopodia, indicating interaction with the substrate surface. On the other hand, the cells in the microcolumn topography show a spreading more similar to the cells on the flat substrates; however, they have actin accumulation in specific areas. The line-like accumulations may suggest that cells are spreading inside the grooves of the topography.

Table 3.8: Statistical significance of the differences between the groups using Mann-Whitney test, for circularity. *** denotes $p < 0.001$, ** denotes $p < 0.01$, * denotes $p < 0.05$ and ns denotes all $p > 0.05$.

	Polished	LIPSS	Microcolumns
Glass	ns	ns	ns
Polished		ns	ns
LIPSS			ns

3.3 Cell behavior on striped topographies

10 μm wide stripes of microcolumn or trench topography were structured on either polished silicon or LIPSS. To generate the patterns, first LIPSS was structured over the whole area, and then the microcolumn stripes were overlaid on the LIPSS pattern. A schematic representation of the structuring pattern is shown in Figure 3.22. SEM images of structured substrates are shown in Figure 3.23.

The width of the microcolumn strips is comparable to the cell body size and was achievable with only one pass of the laser with spot size $\approx$10 μm. Cells transfected with LifeAct were grown for 6 or 24 hours on the structured surfaces, then fixed and imaged with both fluorescence microscopy and SEM. SEM images of cells on these topographies are shown in Figure 3.24. The cells had been growing for 6 hours on the topographies, so these images represent initial spreading. In each of the images, cells still have a circular shape and are interacting with the substrate through lamellipodia-like structures. Some cells are seen spreading out on the flat regions in Figure D. In parts A,B and C, cells seem to be confined to the microcolumn stripe.

Figure 3.25 shows cells growing on the same substrate for 24 hours. In Figure 11, the region of interest (ROI) contains both polished (control) and structured regions. The red line shows the border between the polished region (left) and structured region (right). The inset at the right side represents the topography of the region, LIPSS with microcolumn stripes. Cell alignment to the microcolumns is noticeable at the right side of the image, with the cells accumulating preferentially along the microcolumn stripes. Interestingly, this effect was visible on microcolumn stripes alternating with

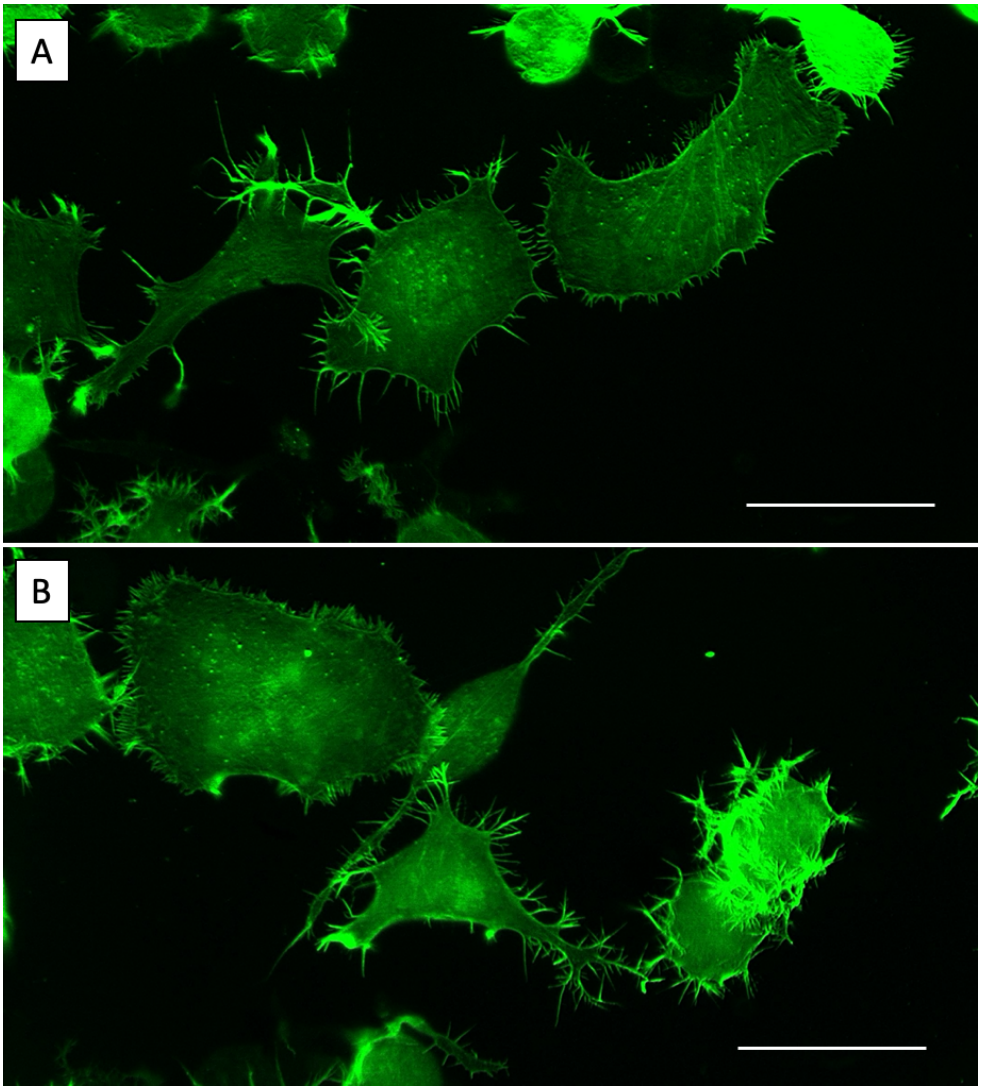

Figure 3.20: :Fluorescence images of cells spreading on polished silicon regions. Cells were expressing LifeAct-EGFP and had been growing in 1% FBS medium for 24 hours. The images were taken with 63X oil objective. All scale bars are 50 μm.

LIPSS, but not those with flat.

The Figure 3.26 below shows the cell alignment to the microcolumn line regions on the structured silicon (Microcolumn lines on LIPSS) compared to the microcolumn trench lines on polished silicon after 24 hours. A and B show cells on the microcolumn trench lines on polished silicon, while C and D show cells on the microcolumn lines on LIPSS topographies. The inset shows representative SEM of substrate, not to scale. The difference in alignment is visible from the images.

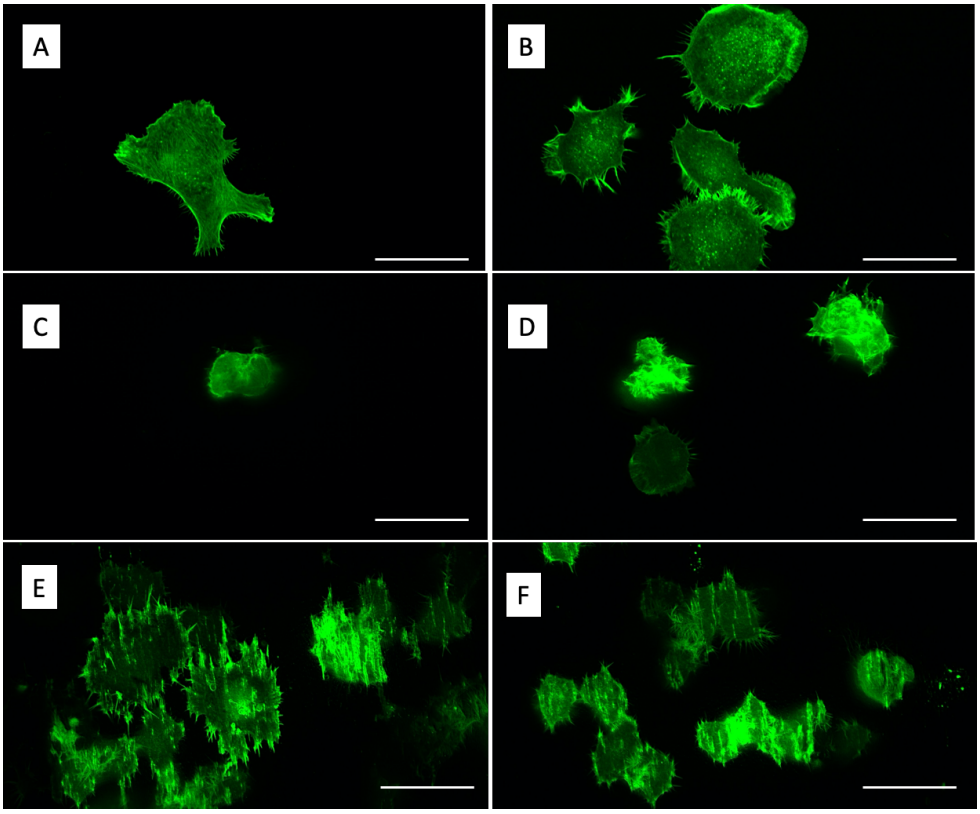

Figure 3.21: Fluorescence images of cells spreading on polished silicon (A,B), LIPSS (C,D) and microcolumn (E,F) topographies. Cells were expressing LifeAct-EGFP and had been growing in 1% FBS medium for 24 hours. The images were taken with 63X oil objective. All scale bars are 50 μm.

When flat regions were available between the microcolumn stripes, cells spread both on flat and microcolumn regions, with no significant preference between the two structures. However, when LIPSS regions were found between the microcolumn stripes, then cells were more likely to be found on the microcolumn stripes. A quantification of the results was done by manual cell counting, by direct comparison of the cell numbers on the different regions. Three different images were used. First, the brightness and contrast of the images was adjusted such that the underlying topography became visible. The positions of the stripes were noted. Then, the cells were manually counted using ImageJ's Cell counter. Cells with more than half of their body on the stripe were considered to be on the stripe (aligned). Finally, the number of cells on the stripes and between the stripes were normalized to the total cell number and shown as a percentage. The results are summarized in the bar graph

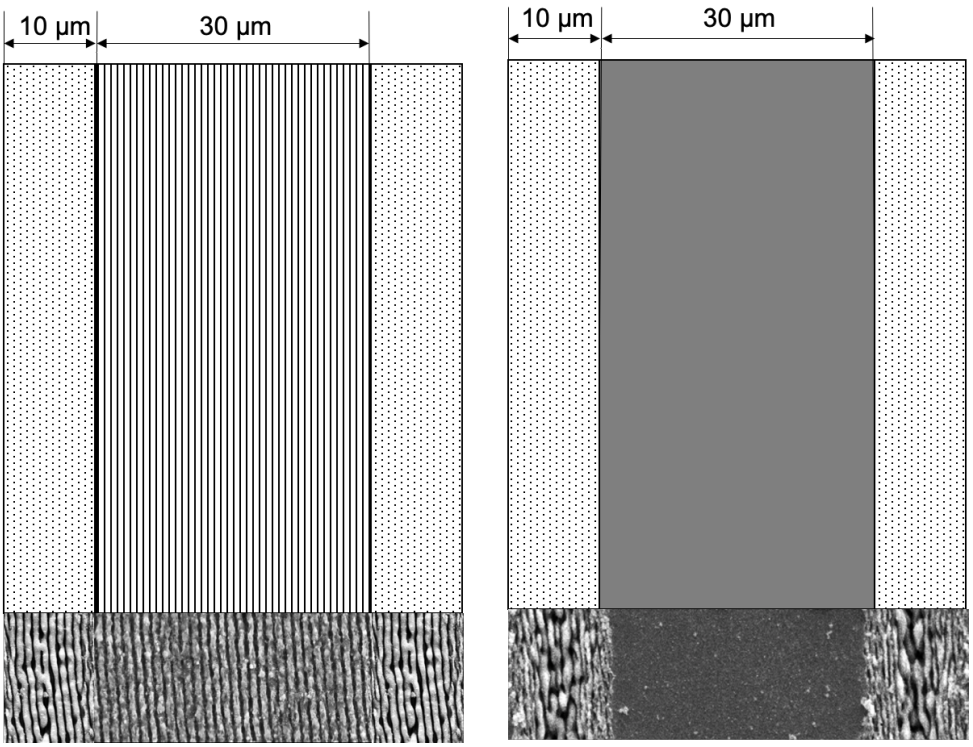

Figure 3.22: :Schematic representation of microcolumn stripe topography alternating with A. LIPSS; B: Flat regions.

in Figures 3.27 3.28 and in Table 3.9.

Table 3.9: The percentage of cells on the topography lines (microcolumn) for microcolumn stripes on LIPSS and for microcolumn stripes on polished silicon topographies.

Microcolumn stripe on LIPSS	64 ± 3 %
Microcolumn stripe on polished	47 ± 3%

It should be noted that these values were not normalized for total area (flat or LIPSS regions are 3 times thicker than the microcolumn regions). The reason is that the usage of 10X objective images and manual cell counting come with inherent errors, as the exact border between the structured and flat or LIPSS regions cannot be well determined. Nevertheless, the cells seem to be almost twice as likely to be found on the microcolumn regions when LIPSS is between the stripes, whereas no effect is seen on the polished regions. Another study found a similar effect of cell alignment

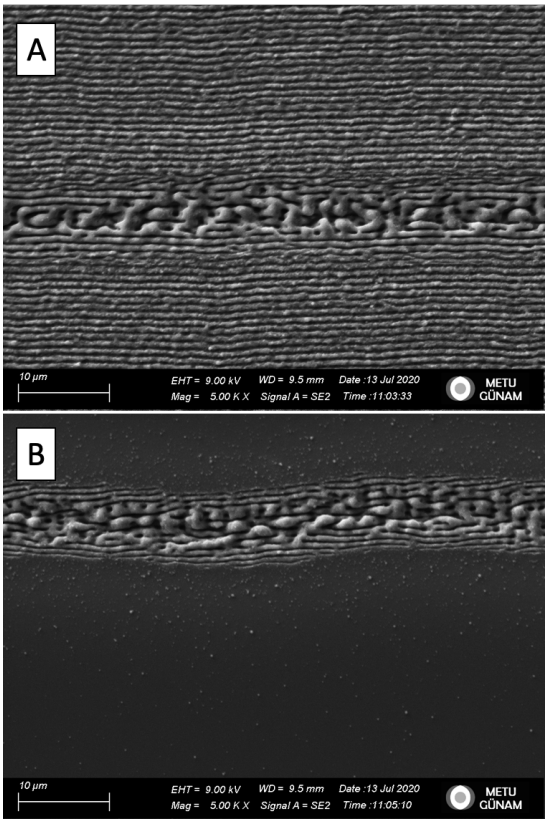

Figure 3.23: SEM images of microcolumn stripe topography alternating with A. LIPSS; B: Flat regions.

when LIPSS regions were present, and no alignment when flat regions were present. It should be noted that another cell line, material and different laser parameters were used [81]. Moreover, in that study, the 10 μm regions were LIPSS with different direction from the 30 μm region. On the other hand, in our study, the 10 μm regions had the same directionality but far less periodicity and more depth. Despite these differences, the lack of alignment effects when flat regions were present was similar in both cases, and suggests more research is needed in order to elucidate the effect of LIPSS topography on the final cell alignment.

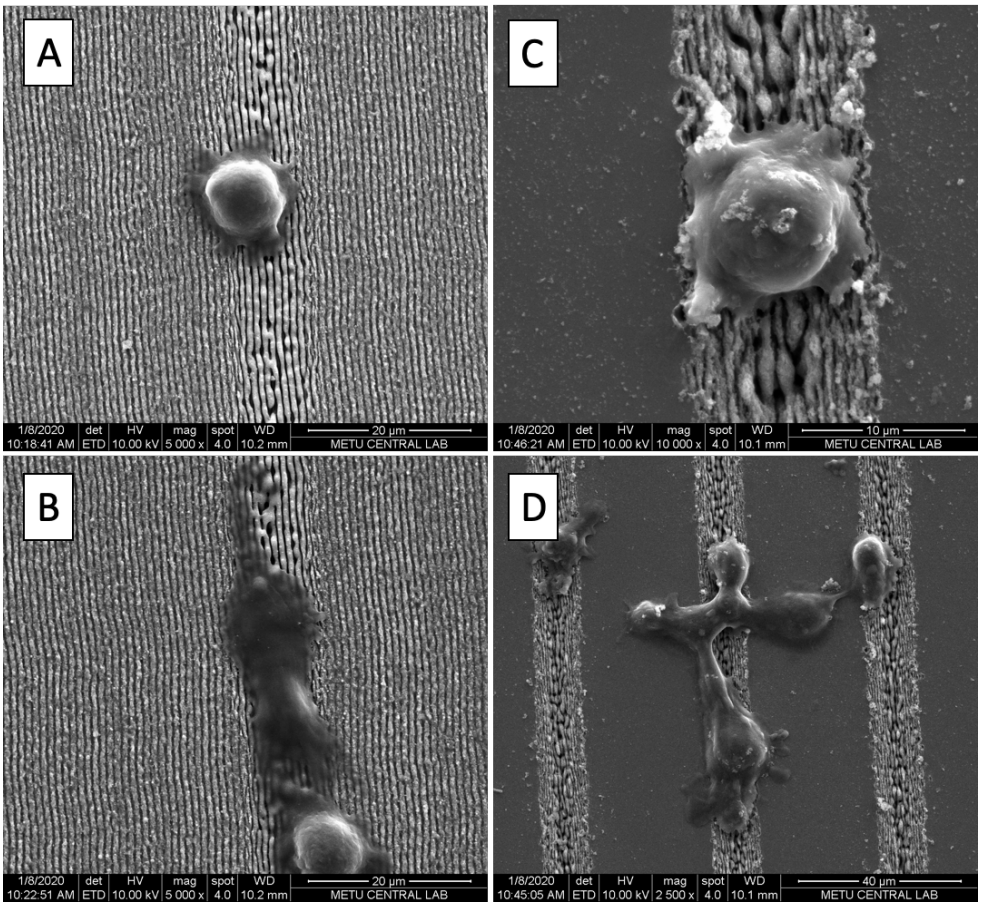

Figure 3.24: SEM images of cells growing on microcolumn stripe topography alternating with LIPSS (A,B); and flat regions (C,D)

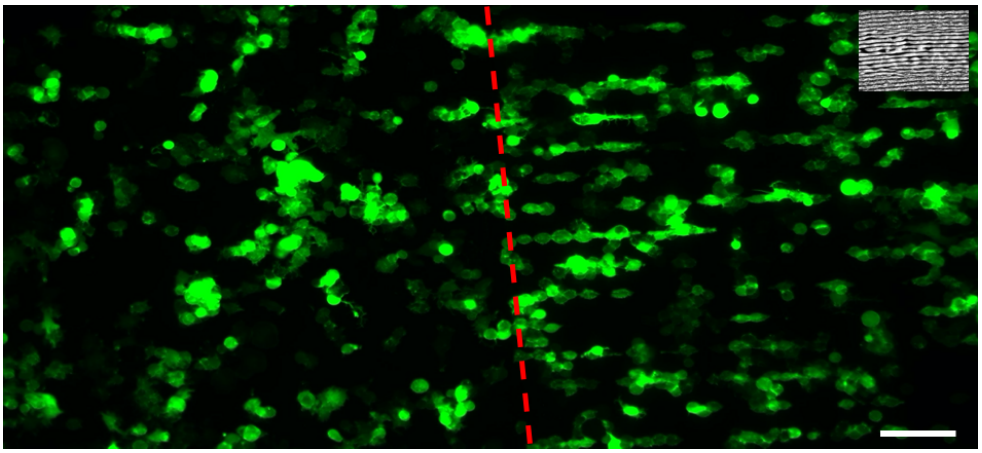

Figure 3.25: Fluorescence microscopy image of cells growing on a region of interest (ROI) containing both polished (control) and structured regions for 24 hours. Scale bar is 100 μm.

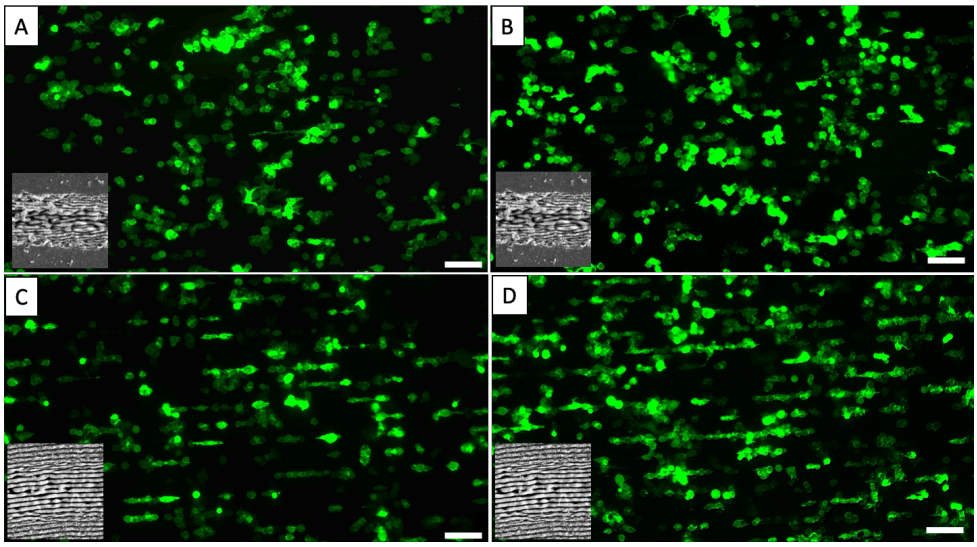

Figure 3.26: 10X fluorescence microscopy images of cells expressing LifeAct-EGFP and grown for 24 hours on microcolumn stripes on flat (A,B) and microcolumn stripes on LIPSS (C,D). All scale bars are 100 μm.

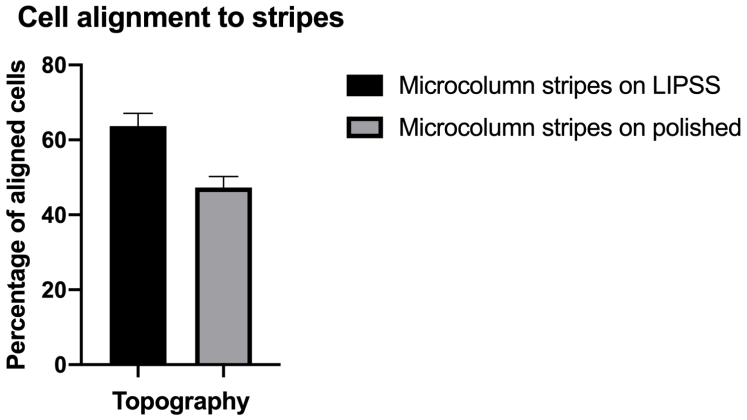

Figure 3.27: Bar graph representing the percentage of cells on the topography lines (microcolumn) and those outside of the topography lines, for microcolumn stripes on LIPSS and for microcolumn stripes on polished silicon. Three separate 10X images were taken into consideration.

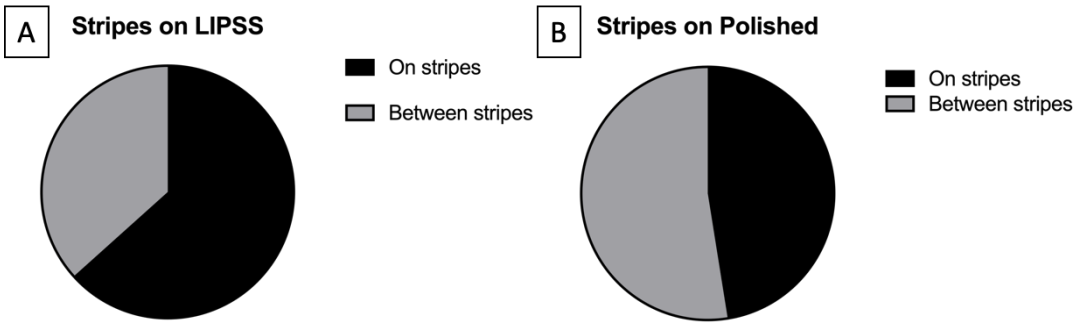

Figure 3.28: Pie chart representing the percentage of cells on the topography lines (microcolumn) and those outside of the topography lines, for microcolumn stripes on LIPSS and for microcolumn stripes on polished silicon. Three separate 10X images were taken into consideration.

CHAPTER 4

CONCLUSION

In this study, the behaviors of Neuro-2a cells on silicon substrates with different topographical features were analyzed. The silicon substrates were structured using femtosecond laser and analyzed using SEM. It was possible to generate LIPSS, microcolumns as well as their combinations. Cells were visualized using transient transfection with fluorescent proteins targeted to the nucleus, membrane or actin cytoskeleton. Fluorescence microscopy, live imaging and SEM was used to observe the cells. Cell shape, numbers and motility were analyzed manually using ImageJ plugins.

On the three different topographies (polished, LIPSS or microcolumns), cells displayed different behaviors at different time points.

Initially, cells were more likely to adhere to structured regions, especially microcolumns, than to polished silicon. Washing the substrates after 3 hours allowed efficient cell patterning on definite areas on the substrate. This patterning preserved for several hours, but cells spread out after 24 hours. Cell motility was different among the three topographies. Cells were fastest on polished silicon and showed anisotropic lamellipodia-like structures similar to cells moving on glass. On the other hand, cells were significantly slower on both structured regions and did not show these lamellipodia. No directionality was observed on LIPSS topographies.

Cell proliferation was decreased in all silicon substrates compared to standard cell culture treated plastic material.

After 24 hours, cells were able to adhere to all topographies, and no significant differences were found in the cell numbers on polished silicon, LIPSS or microcolumns. Cell shape indicators showed some differences among the three silicon substrates and glass. Cell area and perimeter were found to be greater in polished silicon and LIPSS, compared to microcolumn and stripe topographies. No difference was found

in cell circularity among the different substrates. On topographies comprising 10 μm wide microcolumn stripes alternating with polished or LIPSS-structured 30 μm wide regions, cells showed significant preference and confinement to the microcolumn stripes when there was LIPSS between them, but not when there were polished areas between them.

In conclusion, cells displayed differences in adhesion, motility, shape and actin cytoskeleton among the three different topographies. Topography alone was able to modulate a variety of behaviors in Neuro-2a cell line.

Future perspectives involve the further study of the presented results, as well as new directions.

For example, it is not clear why the cells align to microcolumn stripes when they are alternating with LIPSS, but not with polished regions. Longer time-lapse experiments may give hints to this. Furthermore, the effect of the direction of LIPSS relative to the stripes may be studied.

A protocol for Neuro-2a cell differentiation on the silicon substrates may be established, and the effect of the silicon substrates on the differentiation and possibly neurite alignment can be studied. Similarly, different cell types may be studied on laser-structured silicon. Presently, the types of cells studied on laser-structured silicon are very few, leaving room for much research in this area.

On the other hand, the behavior of Neuro-2a and other cells on these substrates may be considered from other points of view. For example, given the importance of focal adhesions in establishing the communication between the cell and substrate, the focal adhesion formation on different topographies may be studied in detail.

Furthermore, the global changes taking place in cells on silicon substrates may be studied with spectroscopic methods such as ATR-FTIR. This method has previously been shown to be able to discriminate between mammalian or bacterial cells receiving various treatments. It would be interesting to see if one can discriminate between cells growing on glass or various silicon topographies using ATR-FTIR spectra and chemometrics. All in all, numerous new leads and further areas of exploration remain.

REFERENCES

[1] P. Kanchanawong, G. Shtengel, A. M. Pasapera, E. B. Ramko, M. W. Davidson, H. F. Hess, and C. M. Waterman, "Nanoscale architecture of integrin-based cell adhesions," *Nature*, vol. 468, no. 7323, pp. 580–584, 2010.

[2] P. K. Mattila and P. Lappalainen, "Filopodia: molecular architecture and cellular functions," *Nature Reviews Molecular Cell Biology*, vol. 9, no. 6, pp. 446–454, 2008.

[3] S. K. Sundaram and E. Mazur, "Inducing and probing non-thermal transitions in semiconductors using femtosecond laser pulses," *Nature Materials*, vol. 1, no. 4, pp. 217–224, 2002.

[4] J. Bonse, S. Baudach, J. Kruger, W. Kautek, and M. Lenzner, "Femtosecond laser ablation of silicon–modification thresholds and morphology," *Applied Physics A*, vol. 74, no. 1, pp. 19–25, 2014.

[5] C. A. Heckman and H. K. Plummer, "Filopodia as sensors," *Cellular Signalling*, vol. 25, no. 11, pp. 2298–2311, 2013.

[6] H. Wolfenson, T. Iskratsch, and M. P. Sheetz, "Early events in cell spreading as a model for quantitative analysis of biomechanical events," *Biophys J*, vol. 107, no. 11, pp. 2508–2514, 2014.

[7] V. Brunetti, G. Maiorano, L. Rizzello, B. Sorce, S. Sabella, R. Cingolani, and P. P. Pompa, "Neurons sense nanoscale roughness with nanometer sensitivity," *Proc Natl Acad Sci U S A*, vol. 107, no. 14, pp. 6264–6269, 2010.

[8] L. Hao, J. Lawrence, Y. F. Phua, K. S. Chian, G. C. Lim, and H. Y. Zheng, "Enhanced human osteoblast cell adhesion and proliferation on 316 LS stainless steel by means of CO2 laser surface treatment," *J Biomed Mater Res B Appl Biomater*, vol. 73, no. 1, pp. 148–156, 2005.

[9] K. K. Tan, C. S. Giam, M. Y. Leow, C. W. Chan, and E. K. Yim, "Differential cell adhesion of breast cancer stem cells on biomaterial substrate with nanotopographical cues," *J Funct Biomater*, vol. 6, no. 2, pp. 241–258, 2015.

[10] S. Mukherjee, S. Dhara, and P. Saha, "Enhancing the biocompatibility of Ti6Al4V implants by laser surface microtexturing: an in vitro study," *The International Journal of Advanced Manufacturing Technology*, vol. 76, no. 1-4, pp. 5–15, 2013.

[11] M. J. Dalby, M. O. Riehle, D. S. Sutherland, H. Agheli, and A. S. Curtis, "Changes in fibroblast morphology in response to nano-columns produced by colloidal lithography," *Biomaterials*, vol. 25, no. 23, pp. 5415–5422, 2004.

[12] N. R. Blumenthal, O. Hermanson, B. Heimrich, and V. P. Shastri, "Stochastic nanoroughness modulates neuron-astrocyte interactions and function via mechanosensing cation channels," *Proc Natl Acad Sci U S A*, vol. 111, no. 45, pp. 16124–16129, 2014.

[13] D. Franco, M. Klingauf, M. Bednarzik, M. Cecchini, V. Kurtcuoglu, J. Gobrecht, D. Poulikakos, and A. Ferrari, "Control of initial endothelial spreading by topographic activation of focal adhesion kinase," *Soft Matter*, vol. 7, no. 16, 2011.

[14] I. Tonazzini, M. Pellegrini, M. Pellegrino, and M. Cecchini, "Interaction of leech neurons with topographical gratings: comparison with rodent and human neuronal lines and primary cells," *Interface Focus*, vol. 4, no. 1, p. 20130047, 2014.

[15] K. Baranes, N. Chejanovsky, N. Alon, A. Sharoni, and O. Shefi, "Topographic cues of nano-scale height direct neuronal growth pattern," *Biotechnol Bioeng*, vol. 109, no. 7, pp. 1791–1797, 2012.

[16] C. Xie, L. Hanson, W. Xie, Z. Lin, B. Cui, and Y. Cui, "Noninvasive neuron pinning with nanopillar arrays," *Nano Lett*, vol. 10, no. 10, pp. 4020–4024, 2010.

[17] S. Oh, C. Daraio, L. H. Chen, T. R. Pisanic, R. R. Finones, and S. Jin, "Significantly accelerated osteoblast cell growth on aligned TiO2 nanotubes," *J Biomed Mater Res A*, vol. 78, no. 1, pp. 97–103, 2006.

[18] L. C. Lee, N. Gadegaard, M. C. de Andres, L. A. Turner, K. V. Burgess, S. J. Yarwood, J. Wells, M. Salmeron-Sanchez, D. Meek, R. O. Oreffo, and M. J. Dalby, "Nanotopography controls cell cycle changes involved with skeletal stem cell self-renewal and multipotency," *Biomaterials*, vol. 116, pp. 10–20, 2017.

[19] K. Das, S. Bose, and A. Bandyopadhyay, "TiO2 nanotubes on Ti: Influence of nanoscale morphology on bone cell-materials interaction," *J Biomed Mater Res A*, vol. 90, no. 1, pp. 225–237, 2009.

[20] A. A. Moe, M. Suryana, G. Marcy, S. K. Lim, S. Ankam, J. Z. Goh, J. Jin, B. K. Teo, J. B. Law, H. Y. Low, E. L. Goh, M. P. Sheetz, and E. K. Yim, "Microarray with micro- and nano-topographies enables identification of the optimal topography for directing the differentiation of primary murine neural progenitor cells," *Small*, vol. 8, no. 19, pp. 3050–3061, 2012.

[21] S. Ankam, M. Suryana, L. Y. Chan, A. A. Moe, B. K. Teo, J. B. Law, M. P. Sheetz, H. Y. Low, and E. K. Yim, "Substrate topography and size determine the fate of human embryonic stem cells to neuronal or glial lineage," *Acta Biomater*, vol. 9, no. 1, pp. 4535–4545, 2013.

[22] R. J. McMurray, N. Gadegaard, P. M. Tsimbouri, K. V. Burgess, L. E. McNamara, R. Tare, K. Murawski, E. Kingham, R. O. Oreffo, and M. J. Dalby, "Nanoscale surfaces for the long-term maintenance of mesenchymal stem cell phenotype and multipotency," *Nat Mater*, vol. 10, no. 8, pp. 637–644, 2011.

[23] E. Sayin, E. T. Baran, and V. Hasirci, "Osteogenic differentiation of adipose derived stem cells on high and low aspect ratio micropatterns," *J Biomater Sci Polym Ed*, vol. 26, no. 18, pp. 1402–1424, 2015.

[24] E. Maffioli, C. Schulte, S. Nonnis, F. Grassi Scalvini, C. Piazzoni, C. Lenardi, A. Negri, P. Milani, and G. Tedeschi, "Proteomic Dissection of Nanotopography-Sensitive Mechanotransductive Signaling Hubs that Foster Neuronal Differentiation in PC12 Cells," *Front Cell Neurosci*, vol. 11, p. 417, 2017.

[25] S. Ankam, B. K. K. Teo, G. Pohan, S. W. L. Ho, C. K. Lim, and E. K. F. Yim, "Temporal Changes in Nucleus Morphology, Lamin A/C and Histone Methyla-

tion During Nanotopography-Induced Neuronal Differentiation of Stem Cells," *Front Bioeng Biotechnol*, vol. 6, p. 69, 2018.

[26] M. J. Dalby, S. J. Yarwood, M. O. Riehle, H. J. Johnstone, S. Affrossman, and A. S. Curtis, "Increasing fibroblast response to materials using nanotopography: morphological and genetic measurements of cell response to 13-nm-high polymer demixed islands," *Exp Cell Res*, vol. 276, no. 1, pp. 1–9, 2002.

[27] E. K. Yim, E. M. Darling, K. Kulangara, F. Guilak, and K. W. Leong, "Nanotopography-induced changes in focal adhesions, cytoskeletal organization, and mechanical properties of human mesenchymal stem cells," *Biomaterials*, vol. 31, no. 6, pp. 1299–1306, 2010.

[28] M. Bani-Yaghoub, R. Tremblay, R. Voicu, G. Mealing, R. Monette, C. Py, K. Faid, and M. Sikorska, "Neurogenesis and neuronal communication on micropatterned neurochips," *Biotechnol Bioeng*, vol. 92, no. 3, pp. 336–345, 2005.

[29] S. Khan and G. Newaz, "A comprehensive review of surface modification for neural cell adhesion and patterning," *J Biomed Mater Res A*, vol. 93, no. 3, pp. 1209–1224, 2010.

[30] A. T. Nguyen, S. R. Sathe, and E. K. Yim, "From nano to micro: topographical scale and its impact on cell adhesion, morphology and contact guidance," *J Phys Condens Matter*, vol. 28, no. 18, p. 183001, 2016.

[31] K. E. Kubow, V. D. Shuklis, D. J. Sales, and A. R. Horwitz, "Contact guidance persists under myosin inhibition due to the local alignment of adhesions and individual protrusions," *Sci Rep*, vol. 7, no. 1, p. 14380, 2017.

[32] M. T. Frey, I. Y. Tsai, T. P. Russell, S. K. Hanks, and Y. L. Wang, "Cellular responses to substrate topography: role of myosin II and focal adhesion kinase," *Biophys J*, vol. 90, no. 10, pp. 3774–3782, 2006.

[33] E. I. Liang, E. J. Mah, A. F. Yee, and M. A. Digman, "Correlation of focal adhesion assembly and disassembly with cell migration on nanotopography," *Integr Biol (Camb)*, vol. 9, no. 2, pp. 145–155, 2017.

[34] B. Kasemo, "Biological surface science," *Current Opinion in Solid State and Materials Science*, vol. 3, no. 5, pp. 451–459, 1998.

[35] C. J. Wilson Clegg, R.E., Leavesley, D.I., Pearcy, M., "Mediation of Biomaterial–Cell Interactions by Adsorbed Proteins: A Review," *Tissue Eng*, vol. 11, no. 1/2, 2005.

[36] A. Ranella, M. Barberoglou, S. Bakogianni, C. Fotakis, and E. Stratakis, "Tuning cell adhesion by controlling the roughness and wettability of 3D micro/nano silicon structures," *Acta Biomater*, vol. 6, no. 7, pp. 2711–2720, 2010.

[37] K. R. Kam, L. A. Walsh, S. M. Bock, J. D. Ollerenshaw, R. F. Ross, and T. A. Desai, "The effect of nanotopography on modulating protein adsorption and the fibrotic response," *Tissue Eng Part A*, vol. 20, no. 1-2, pp. 130–138, 2014.

[38] M. S. Lord, B. G. Cousins, P. J. Doherty, J. M. Whitelock, A. Simmons, R. L. Williams, and B. K. Milthorpe, "The effect of silica nanoparticulate coatings on serum protein adsorption and cellular response," *Biomaterials*, vol. 27, no. 28, pp. 4856–4862, 2006.

[39] P. Decuzzi and M. Ferrari, "Modulating cellular adhesion through nanotopography," *Biomaterials*, vol. 31, no. 1, pp. 173–179, 2010.

[40] E. Stratakis, A. Ranella, M. Farsari, and C. Fotakis, "Laser-based micro/nanoengineering for biological applications," *Progress in Quantum Electronics*, vol. 33, no. 5, pp. 127–163, 2009.

[41] J. Heller, J. W. Bartha, C. C. Poon, and A. C. Tam, "Temperature dependence of the reflectivity of silicon with surface oxide at wavelengths of 633 and 1047 nm," *Applied Physics Letters*, vol. 75, no. 1, pp. 43–45, 1999.

[42] J. C. Weeber, J. R. Krenn, A. Dereux, B. Lamprecht, Y. Lacroute, and J. P. Goudonnet, "Near-field observation of surface plasmon polariton propagation on thin metal stripes," *Physical Review B*, vol. 64, no. 4, 2001.

[43] M. A. Green and M. J. Keevers, "Optical properties of intrinsic silicon at 300 K," *Progress in Photovoltaics: Research and Applications*, vol. 3, no. 3, pp. 189–192, 1995.

[44] M. S. Brown and C. B. Arnold, "Fundamentals of Laser-Material Interaction and Application to Multiscale Surface Modification," in *Laser Precision Micro-*

fabrication (K. Sugioka, M. Meunier, and A. Piqué, eds.), pp. 91–120, Berlin, Heidelberg: Springer Berlin Heidelberg, 2010.

[45] B. Öktem, I. Pavlov, S. Ilday, H. Kalaycıoğlu, A. Rybak, S. Yavaş, M. Erdoğan, and F. Ö. Ilday, "Nonlinear laser lithography for indefinitely large-area nanostructuring with femtosecond pulses," *Nature Photonics*, vol. 7, no. 11, pp. 897–901, 2013.

[46] P. Premnath, A. Tavangar, B. Tan, and K. Venkatakrishnan, "Tuning cell adhesion by direct nanostructuring silicon into cell repulsive/adhesive patterns," *Exp Cell Res*, vol. 337, no. 1, pp. 44–52, 2015.

[47] I. Pavlov, O. Yavuz, G. Makey, O. Toke, and O. Ilday, "Switching between normal and anomalous Laser Induced Periodic Surface Structures," 2017.

[48] J. Bonse, S. Hohm, S. V. Kirner, A. Rosenfeld, and J. Kruger, "Laser-Induced Periodic Surface Structures— A Scientific Evergreen," *IEEE Journal of Selected Topics in Quantum Electronics*, vol. 23, no. 3, 2017.

[49] T. Tomita, R. Kumai, S. Matsuo, S. Hashimoto, and M. Yamaguchi, "Cross-sectional morphological profiles of ripples on Si, SiC, and HOPG," *Applied Physics A*, vol. 97, no. 2, pp. 271–276, 2009.

[50] A. Y. Vorobyev Guo, C., "Direct femtosecond laser surface nano/microstructuring and its applications," *Laser Photonics Rev.*, vol. 7, no. 3, pp. 385–407, 2013.

[51] J. Bonse, A. Rosenfeld, and J. Krüger, "On the role of surface plasmon polaritons in the formation of laser-induced periodic surface structures upon irradiation of silicon by femtosecond-laser pulses," *Journal of Applied Physics*, vol. 106, no. 10, 2009.

[52] V. Oliveira, S. Ausset, and R. Vilar, "Surface micro/nanostructuring of titanium under stationary and non-stationary femtosecond laser irradiation," *Applied Surface Science*, vol. 255, no. 17, pp. 7556–7560, 2009.

[53] F. Keilmann and Y. H. Bai, "Periodic surface structures frozen into CO2 laser-melted quartz," *Applied Physics A*, vol. 29, no. 1, pp. 9–18, 1982.

[54] H. M. van Driel, J. E. Sipe, and J. F. Young, "Laser-Induced Periodic Surface Structure on Solids: A Universal Phenomenon," *Physical Review Letters*, vol. 49, no. 26, pp. 1955–1958, 1982.

[55] A. A. Ionin, S. I. Kudryashov, S. V. Makarov, A. A. Rudenko, L. V. Seleznev, D. V. Sinitsyn, and V. I. Emel'yanov, "Nonlinear optical dynamics during femtosecond laser nanostructuring of a silicon surface," *Laser Physics Letters*, vol. 12, no. 2, 2015.

[56] I. Gnilitskyi, T. J. Y. Derrien, Y. Levy, N. M. Bulgakova, T. Mocek, and L. Orazi, "High-speed manufacturing of highly regular femtosecond laser-induced periodic surface structures: physical origin of regularity," *Scientific Reports*, vol. 7, no. 1, p. 8485, 2017.

[57] W. Hendrikson, W. Masman-Bakker, B. van Bochove, J. Skolski, J. Eichstadt, B. Koopman, C. van Blitterswijk, D. Grijpma, G. W. Romer, L. Moroni, and J. Rouwkema, "Mold-Based Application of Laser-Induced Periodic Surface Structures (LIPSS) on Biomaterials for Nanoscale Patterning," *Macromol Biosci*, vol. 16, no. 1, pp. 43–49, 2016.

[58] M. Oberringer, E. Akman, J. Lee, W. Metzger, C. K. Akkan, E. Kacar, A. Demir, H. Abdul-Khaliq, N. Putz, G. Wennemuth, T. Pohlemann, M. Veith, and C. Aktas, "Reduced myofibroblast differentiation on femtosecond laser treated 316LS stainless steel," *Mater Sci Eng C Mater Biol Appl*, vol. 33, no. 2, pp. 901–908, 2013.

[59] H. Kenar, E. Akman, E. Kacar, A. Demir, H. Park, H. Abdul-Khaliq, C. Aktas, and E. Karaoz, "Femtosecond laser treatment of 316L improves its surface nanoroughness and carbon content and promotes osseointegration: An in vitro evaluation," *Colloids Surf B Biointerfaces*, vol. 108, pp. 305–312, 2013.

[60] T. Nuutinen, M. Silvennoinen, K. Paivasaari, and P. Vahimaa, "Control of cultured human cells with femtosecond laser ablated patterns on steel and plastic surfaces," *Biomed Microdevices*, vol. 15, no. 2, pp. 279–288, 2013.

[61] A. M. Alshehri, S. Hadjiantoniou, R. J. Hickey, Z. Al-Rekabi, J. L. Harden, A. E. Pelling, and V. R. Bhardwaj, "Selective cell adhesion on femtosecond laser-

microstructured polydimethylsiloxane," *Biomed Mater*, vol. 11, no. 1, p. 15014, 2016.

[62] E. Rebollar, I. Frischauf, M. Olbrich, T. Peterbauer, S. Hering, J. Preiner, P. Hinterdorfer, C. Romanin, and J. Heitz, "Proliferation of aligned mammalian cells on laser-nanostructured polystyrene," *Biomaterials*, vol. 29, no. 12, pp. 1796–1806, 2008.

[63] A. Cunha Zouani OF, Plawinski L, Botelho do Rego AM, Almeida A, Vilar R, Durrieu MC., "Human mesenchymal stem cell behavior on femtosecond laser-textured Ti-6Al-4V surfaces," *Nanomedicine (Lond).*, vol. 10, no. 5, pp. 725–739, 2015.

[64] C. McDaniel, O. Gladkovskaya, A. Flanagan, Y. Rochev, and G. M. O'Connor, "In vitro study on the response of RAW264.7 and MS-5 fibroblast cells on laser-induced periodic surface structures for stainless steel alloys," *RSC Advances*, vol. 5, no. 53, pp. 42548–42558, 2015.

[65] O. Raimbault, S. Benayoun, K. Anselme, C. Mauclair, T. Bourgade, A. M. Kietzig, P. L. Girard-Lauriault, S. Valette, and C. Donnet, "The effects of femtosecond laser-textured Ti-6Al-4V on wettability and cell response," *Mater Sci Eng C Mater Biol Appl*, vol. 69, pp. 311–320, 2016.

[66] Y. Sato, M. Tsukamoto, T. Shinonaga, and T. Kawa, "Femtosecond laser-induced periodic nanostructure creation on PET surface for controlling of cell spreading," *Applied Physics A*, vol. 122, no. 3, 2016.

[67] R. A. Barb, C. Hrelescu, L. Dong, J. Heitz, J. Siegel, P. Slepicka, V. Vosmanska, V. Svorcik, B. Magnus, R. Marksteiner, M. Schernthaner, and K. Groschner, "Laser-induced periodic surface structures on polymers for formation of gold nanowires and activation of human cells," *Applied Physics A*, vol. 117, no. 1, pp. 295–300, 2014.

[68] C. Yiannakou, C. Simitzi, A. Manousaki, C. Fotakis, A. Ranella, and E. Stratakis, "Cell patterning via laser micro/nano structured silicon surfaces," *Biofabrication*, 2017.

[69] Y. W. Fan, F. Z. Cui, L. N. Chen, Y. Zhai, Q. Y. Xu, and I. S. Lee, "Adhesion of neural cells on silicon wafer with nano-topographic surface," *Applied Surface Science*, vol. 187, no. 3-4, pp. 313–318, 2002.

[70] F. Gentile, R. La Rocca, G. Marinaro, A. Nicastri, A. Toma, F. Paonessa, G. Cojoc, C. Liberale, F. Benfenati, E. di Fabrizio, and P. Decuzzi, "Differential cell adhesion on mesoporous silicon substrates," *ACS Appl Mater Interfaces*, vol. 4, no. 6, pp. 2903–2911, 2012.

[71] F. Gentile, R. Medda, L. Cheng, E. Battista, P. E. Scopelliti, P. Milani, E. A. Cavalcanti-Adam, and P. Decuzzi, "Selective modulation of cell response on engineered fractal silicon substrates," *Sci Rep*, vol. 3, p. 1461, 2013.

[72] L. Micholt, A. Gartner, D. Prodanov, D. Braeken, C. G. Dotti, and C. Bartic, "Substrate topography determines neuronal polarization and growth in vitro," *PLoS ONE*, vol. 8, no. 6, p. e66170, 2013.

[73] S.-W. Kuo, H.-I. Lin, J. Hui-Chun Ho, Y.-R. V. Shih, H.-F. Chen, T.-J. Yen, and O. K. Lee, "Regulation of the fate of human mesenchymal stem cells by mechanical and stereo-topographical cues provided by silicon nanowires," *Biomaterials*, vol. 33, no. 20, pp. 5013–5022, 2012.

[74] Y. L. Khung, G. Barritt, and N. H. Voelcker, "Using continuous porous silicon gradients to study the influence of surface topography on the behaviour of neuroblastoma cells," *Experimental Cell Research*, vol. 314, no. 4, pp. 789–800, 2008.

[75] E. J. Tocce, V. K. Smirnov, D. S. Kibalov, S. J. Liliensiek, C. J. Murphy, and P. F. Nealey, "The ability of corneal epithelial cells to recognize high aspect ratio nanostructures," *Biomaterials*, vol. 31, no. 14, pp. 4064–4072, 2010.

[76] V. S. Polikov, P. A. Tresco, and W. M. Reichert, "Response of brain tissue to chronically implanted neural electrodes," *J Neurosci Methods*, vol. 148, no. 1, pp. 1–18, 2005.

[77] J. Riedl, A. H. Crevenna, K. Kessenbrock, J. H. Yu, D. Neukirchen, M. Bista, F. Bradke, D. Jenne, T. A. Holak, Z. Werb, M. Sixt, and R. Wedlich-Soldner,

"Lifeact: a versatile marker to visualize F-actin," *Nature Methods*, vol. 5, no. 7, pp. 605–607, 2008.

[78] A. Y. Vorobyev, J. Neev, C. Guo, S. Nolte, A. Heisterkamp, and R. P. Trebino, "Femtosecond laser surface structuring of biocompatible metals," 2009.

[79] X. Wang, C. A. Ohlin, Q. Lu, and J. Hu, "Cell directional migration and oriented division on three-dimensional laser-induced periodic surface structures on polystyrene," *Biomaterials*, vol. 29, no. 13, pp. 2049–2059, 2008.

[80] K. Wallat, D. Dörr, R. Le Harzic, F. Stracke, D. Sauer, M. Neumeier, A. Kovtun, H. Zimmermann, and M. Epple, "Cellular reactions toward nanostructured silicon surfaces created by laser ablation," *Journal of Laser Applications*, vol. 24, no. 4, 2012.

[81] M. Martinez-Calderon, M. Manso-Silvan, A. Rodriguez, M. Gomez-Aranzadi, J. P. Garcia-Ruiz, S. M. Olaizola, and R. J. Martin-Palma, "Surface micro- and nano-texturing of stainless steel by femtosecond laser for the control of cell migration," *Sci Rep*, vol. 6, p. 36296, 2016.

[82] A. Beliveau, G. Thomas, J. Gong, Q. Wen, and A. Jain, "Aligned Nanotopography Promotes a Migratory State in Glioblastoma Multiforme Tumor Cells," *Sci Rep*, vol. 6, p. 26143, 2016.

[83] M. Hart, J. Lauer, M. Selig, M. Hanak, B. Walters, and B. Rolauffs, "Shaping the Cell and the Future: Recent Advancements in Biophysical Aspects Relevant to Regenerative Medicine," *Journal of Functional Morphology and Kinesiology*, vol. 3, no. 1, 2017.

[84] S. Tojkander, G. Gateva, and P. Lappalainen, "Actin stress fibers–assembly, dynamics and biological roles," *J Cell Sci*, vol. 125, no. Pt 8, pp. 1855–1864, 2012.